Universität Hamburg
DER FORSCHUNG | DER LEHRE | DER BILDUNG

Ablation Plume Dynamics of DIVE Ablation at Water-Air Interfaces

Master Thesis in Physics

Kristina Strahlendorff

Universität Hamburg

1st reviewer: Prof. Dr. R.J. Dwayne Miller
2nd reviewer: Dr. Christian Kränkel

March 2nd 2016

This thesis was written at the
Max Planck Institute for the Structure and Dynamics of Matter
Luruper Chaussee 149
22761 Hamburg

Abstract

Medical lasers can significantly contribute to minimal invasive procedures in surgery, since lasers can basically cut at the level of a single cell. However, ablation of tissue with a laser involves damage of the surrounding tissue, induced by thermal effects and shock wave propagation. The Picosecond InfraRed Laser (PIRL) drives the ablation of tissue faster than thermal and shock wave propagation can occur in the surrounding tissue. Furthermore, the pulses are within a suitable energy regime and have a picosecond pulse length so that ionization of the tissue is avoided. The infrared PIRL wavelength of 2.96 µm is highly absorbed by the water, which leads to a phase transition from liquid to gas phase. This phase transition drives the formation of a plume consisting of the material from the ablated sample. Important characteristics of the ablation plume are spatial distribution, velocity and density profile, which are providing information about the plume.

In this thesis, a Mach-Zehnder interferometer was set up and a computer code for the analysis developed and used. To verify the functionality of the interferometer and the analysis code a known sample was analyzed, firstly. Afterwards, the spatial distribution of the plume has been evaluated as well as the velocity of the plume. Therefore, a pump-probe experiment was set up, where the PIRL creates the plume which is analyzed by a nanosecond laser based interferometer. The interferometer is working at a spatial resolution of 3 µm and temporal resolution of a few nanoseconds. For resolving the dynamics, the plume was imaged at different times after creation concluding in a velocity of $v_{plume} = 1.16\,\mathrm{km/s}$.

Zusammenfassung

Medizinische Laser können wesentlich zu minimalinvasiven Verfahren in der Chirurgie beitragen, da Laser auf der Ebene einer einzelnen Zelle schneiden können. Jedoch verursacht die Ablation von biologischen Proben mit einem Laser eine Schädigung des umgebenden Gewebes, hervorgerufen durch thermische Effekte und Schockwellenausbreitung. Der Pikosekunden InfraRot Laser (PIRL) ablatiert die Probe schneller als Wärme- und Schockwellenausbreitung in dem umgebenden Gewebe auftreten können. Darüber hinaus ist die Länge der Pikosekunden-Laserpulse groß genug und liegen im geeigneten Energiebereich, dass die Ionisation des Gewebes zu vermeiden. Zudem wird die PIRL-Wellenlänge stark vom Wasser absorbiert, was dann dazu führt, dass ein Phasenübergang von flüssig zu gasförmig auftritt. Dieser Phasenübergang treibt die Bildung einer Ablationswolke (eng. "ablation plume"), die aus dem Material der ablatierten Probe besteht. Wichtige Eigenschaften dieser Ablationswolke sind die räumliche Verteilung, die Geschwindigkeit und das Dichteprofil, welche Informationen über die Ablationswolke liefern.

Im Rahmen dieser Masterarbeit wurde ein Mach-Zehnder-Interferometer aufgebaut und ein Computer Analyse Programms entwickelt. Um die Funktionalität des Interferometers und des Analyse Codes zu überprüfen, wurde zunächst eine bekannten Probe analysiert. Anschließend wurde die räumliche Verteilung sowie die Geschwindigkeit der Ablationswolke untersucht. Um dies zu realisieren wurde ein "Pump-Probe"-Experiment durchgeführt, bei dem der PIRL die Ablationswolke erzeugt, die mittels eines Nanosekunden basierten Laser-Interferometers mit einer räumlichen Auflösung von 3 µm und einer zeitliche Auflösung von wenigen Nanosekunden analysiert wird. Um die Dynamik der Ablationswolke zu ermitteln wurde diese zu verschiedenen Zeiten nach der Erzeugung abgebildet. Daraus wurde eine Geschwindigkeit von $v_{plume} = 1{,}16\,\mathrm{km/s}$ ermittelt.

Contents

List of Figures

List of Tables

1 Introduction and Motivation

Since the laser has been developed in the 1960s, it finds applications in various fields in daily life, in industry, natural science, and medicine. After CO_2 lasers were used for surgery over a few decades, lasers with distinct special spectral and temporal properties now allow to cut even at a single cell level. By choosing the suitable laser wavelength the laser is also capable of targeting different tissue types selectively due to its different spectral absorption of the laser light. Therefore, lasers are now a powerful tool for surgery [1]. However, ablation of tissue with a laser involves damage of the surrounding tissue, induced by thermal effects and shock waves [2]. The laser parameters, type of laser-tissue interaction and type of tissue determine the characteristics of the residual tissue damage. The interaction of the laser with the tissue is classified into five types, depending on exposure time and power density, namely photochemical interaction, thermal interaction, photo-ablation, plasma-induced ablation and photo-disruption [4].

A new mechanism for laser induced ablation using desorption by impulsive vibrational excitation (DIVE) via a picosecond infrared laser (PIRL) had been developed by Franjic and Miller [1, 6, 8]. Here, a highly absorbed pulse tuned to the infrared active vibrations of water is used for the ablation [1]. The total absorbed energy is converted to translational motion rather than into thermal and acoustic transport, thus damage is avoided. This is caused by the adequate short duration of the PIRL-pulses, which are yet long enough and in the suitable energy regime, that a plasma formation that generates ionizing radiation effects is prevented [5].

Specifically, the PIRL is tuned to the vibrational stretch of the water molecules that has an absorption in excess of 10^4 cm^{-1}. The high absorption leads to translational motion of water such that the water within the absorption volume is transferred into gas phase [6]. This phase transition drives the formation of a plume consisting of the material from the ablated sample. Because the ablated fragments are mostly still intact, DIVE-ablation can also be used for the extraction of e.g. proteins [5]. Important characteristics of the plume are spatial distribution, velocity and density profile, which provides information about the dynamics of the plume [7]. This in turn can be used to increase the efficiency of e.g. protein extraction and enhance the coupling to mass spectrometry.

In this thesis, a Mach-Zehnder-Interferometer is set up and a code for the analysis has been developed for measuring phase differences which provides information about spatial distribution of the investigated sample. First, a known sample has been examined to confirm the functionality of the interferometer and the analysis code. Afterwards the spatial distribution and the velocity of ablation plumes was investigated. For a time resolved investigation of the plume, a pump probe experiment was set up. The the PIRL acts as the pump laser to create the plume, which is examined by an interferometer. Different time delays between PIRL pulse and interferometer pulse were set to obtain the velocity of the plume expansion. Temporal and spatial resolution are dependent on the pulse duration of the interference pulse and the fringe space of the interferometer pattern. The pulse duration of the used microchip laser is 1.5 ns and the half width of the fringes is 3 µm.

2 Theory

2.1 DIVE-Ablation

Desorption by Impulsive Vibrational Excitation (DIVE) is a mechanism which drives liquid water into gas phase through laser light absorption. Water has a special behavior due to its disordered three-dimensional hydrogen bond network which couples the water molecules [8]. It has been found by Cowan et al. [9] and confirmed by Vodopyanov et al. [10], Schwarzer et al. [11] and Schäfer et al. [12], that water has ultrafast relaxation of the O-H stretch vibration at $3400\,\mathrm{cm}^{-1}$ and hence ultrafast energy redistribution in the hydrogen bond network. The intermolecular liberations of the hydrogen bond network and the energy transfer between vibrational excited O-H stretching modes occur within a time scale of 200 fs and complete thermalization happens within 1 ps [9]. The absorption coefficient of water in the infrared is high [8]. Due to its ability to localize and thermalize vibrational excitations for high absorbed optical energy densities on an ultrafast time scale, impulsive superheating is possible for water in the condensed phase, which drives a rapid phase transition from liquid to gas phase [8]. By choosing a pulse duration which is longer than or equal to the thermalization time of the vibrational excitation but shorter than the thermal and acoustic relaxation times of the excited volume, the optical energy is most efficiently coupled to the thermally induced phase transition [8]. Molecules that are excited by the laser radiation undergo a direct transition from the condensed phase to gas phase [13].

2.2 Laser Tissue Interactions

When a laser interacts with tissue, the different mechanisms that occur are attributed to the specific laser parameters and the characteristics of the tissue [4]. The wavelength dependent coefficients of reflection, absorption and scattering are the most important optical properties of tissue, because they determine the transmission of the laser light through the tissue. The parameters that characterize the laser radiation are the wavelength, exposure time, applied energy, focal spot size, energy density and power density. The exposure time directly determines the type of interaction. The interaction is classified into five categories, which were mentioned above, namely photochemical interaction, thermal interaction, photoablation, plasma-induced ablation and photodisruption. The

energy range for these interactions approximately vary between $1\,\mathrm{J/cm^2}$ and $1000\,\mathrm{J/cm^2}$, whereas the power density varies over 15 orders of magnitude. This is shown in figure 2.1, for the applied power density in dependence of exposure time.

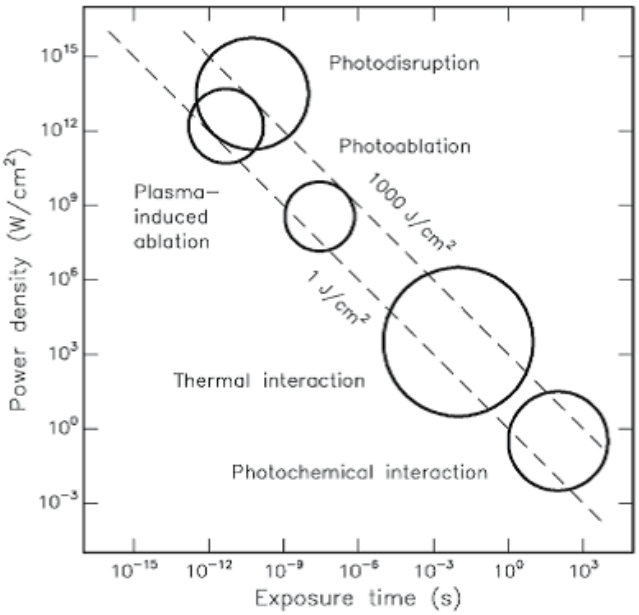

Figure 2.1: Map of laser-tissue interactions dependent on applied power density in relation to exposure time. The diagonals show a constant energy fluence at $1\,\mathrm{J/cm^2}$ and $1000\,\mathrm{J/cm^2}$. The circles give only a rough estimate of the associated laser parameters. Modified from Boulnois (1986) [4].

The five different interactions can be roughly associated to five time sections. By shortening the exposure time, the power density is increased for the specific interaction. The difference between the photodisruption and the plasma-induced ablation is that plasma-induced ablation is based on ionization and the photodisruption is a primarily mechanical effect. Since the relation between the power density and the exposure time is reciprocal, the same energy density is required for any interaction type, which leads to the fact that the main parameter for the interaction type is the exposure time [4, 14]. Since the DIVE-mechanism is a photoablative process, the following subsection only focuses on this interaction type.

2.2.1 Photoablation

Below a certain radiation threshold of about 10^7-$10^8\,\mathrm{W/cm^2}$ and a laser pulse duration in the nanosecond range, photoablation does occurs. The absorbed energy of a single laser pulse is not sufficient to vaporize the irradiated tissue volume. Heat transfer into the non-irradiated regions can be neglected because the ablated material absorbs most of the energy, hence the ablation process is non-thermal [14]. Up to a certain saturation

limit, the pulse energy determines the ablation depth, and thus the tissue removal depth per pulse [4]. The energy to vaporize the material is approximately equal to the absorbed energy for all wavelengths. Therefore, the photoablation is a collective phenomenon. This means that a large absorption coefficient is required for evaporating the tissue [14]. To describe the dependence of the ablated depth on the incident laser intensity, Lambert Beer's law can be used [3] which is given by

$$I(z) = I_0 e^{-\alpha z}. \tag{2.1}$$

Here I_0 denotes the incident laser intensity, α the absorption coefficient of the tissue and z the optical axis. Differentiation in respect to z leads to the evaluation of the intensity decrease

$$-\frac{\partial I}{\partial z} = \alpha I(z). \tag{2.2}$$

As mentioned before, ablation only takes place above a certain power density thus the value αI needs to be above the threshold.
Since tissue does not absorb the energy homogeneously but exhibits a strong scattering behavior, the calculation of the fluence is more complex [14]. Generally, soft biological tissue can be considered as an assembly of cells that reside in and is attached to an extracellular matrix [7]. Soft biological tissue consists, by mass, mostly of water (55-99%). In the visible range, water acts nearly transparent but the absorption rises rapidly in the infrared and has some absorption peaks as shown in fig.2.2, located at $\lambda = 0.96$, 1.44, 1.95, 2.94, 4.68 , and 6.1 µm [7].

Figure 2.2: Liquid water absorption spectrum from the deep UV to the EHF(extremely high frequency) [15].

Compared to the visible range, the absorption of water at $\lambda = 2.94$ µm is six orders of mag-

nitude increased, with an absorption coefficient of $\mu_\alpha = 12\,000\,\mathrm{cm}^{-1}$. The high absorption of the vibrational stretch mode ensures that the deposition of energy in the longitudinal direction is localized within less than 1 µm. The limitation of the ablation depth is in a micrometer scale, dependent on the thickness of a single cell [7, 13]. Through the hydrogen bond network, the excited vibrational modes couple to the O-H translational motion on a sub-picosecond timescale, effecting a direct coupling of the absorbed energy to the translational motion that is needed to drive the ablation process [9].

2.2.2 PIRL

The picosecond infrared laser (PIRL) is designed to operate in the DIVE-regime and has a wavelength of λ =2.96 µm with a pulse duration of 105 ps, leading to a maximal absorption in liquid water on ultrashort time scales. Since the pulse is shorter than the thermal and acoustic relaxation but long enough to transfer the optical energy into heat, hydrated biological tissues can precisely be ablated in single cell dimensions without damaging the surrounding tissue [5]. The ablation process is faster than nucleation growth or energy transfer to adjacent tissue [6]. The high absorption leads to translational motion of the hydrogen that consequently acts like a propellant that drives the ablation volume into gas phase. Thermal fragmentation during the ablation is avoided because the timescale of the ablation process is faster than even collisional exchange of the water molecules [5]. Therefore, the PIRL can also be used for ablation of entire intact proteins [6].
For creating the PIRL pulse with a wavelength of 2.96 µm, an optical parametric amplifier (OPA 2.2.3) is used. The OPA is pumped by a 140 ps long pulse from a Nd:YLF regenerative amplifier at a wavelength of $\lambda = 1053$ nm and seeded from an actively mode-locked Nd:YLF laser. The seed of the OPA is a CW distributive feedback (DFB) fiber coupled laser diode at a wavelength of $\lambda = 1635$ nm as shown in fig.2.3 [8, 16].

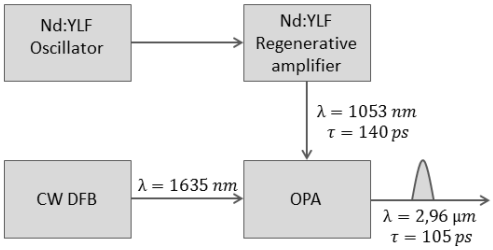

Figure 2.3: Scheme of PIRL laser by Kresimir Franjic and R.J.Dwayne Miller [8]. The optical parametric amplifier (OPA) is seeded with a CW distributed feedback (DFB) fiber coupled laser diode at a wavelength of $\lambda = 1635$ nm and pumped by a pulse from the Nd:YLF regenerative amplifier with $\lambda = 1053$nm and 140 ps pulse length, which is seeded from an actively mode-locked Nd:YLF laser oscillator.

2.2.3 Optical Parametric Amplification

An optical parametric amplifier (OPA) is a nonlinear device, in which a laser beam with high intensity and frequency amplifies a laser beam with less intensity and frequency. Due to conservation of energy and momentum, a third laser beam is created [17]. Figure 2.4 shows the principle of the optical parametric amplification.

Figure 2.4: Scheme of optical parametric amplification. The signal, also called seed, is amplified by the pump within a nonlinear crystal, where due to energy and momentum conservation a third beam is created, called idler [17].

The laser with the higher energy and the central frequency ω_p is called pump, the amplified wave with central frequency ω_s is called signal and the generated wave with central frequency ω_i is called idler. For the PIRL, the idler is the wave of interest because it provides the required wavelength of 2.96 µm if the pump wavelength is 1053 nm and the seed wavelength is 1635 nm. In some OPAs, the signal and pump do not superimpose in the crystal as shown in fig. 2.4 but under an angle, wherefore these types of OPA are called noncollinear optical parametric amplification (NOPA) [18]. The conservation of energy is given by

$$\hbar\omega_p = \hbar\omega_s + \hbar\omega_i. \tag{2.3}$$

Hence the interaction of pump, signal and idler is effective, the conservation of momentum

$$\hbar\vec{k}_p = \hbar\vec{k}_s + \hbar\vec{k}_i \tag{2.4}$$

must be fulfilled, where $\vec{k}_p$, $\vec{k}_s$ and $\vec{k}_i$ are the wave vectors of each pump, signal and idler [19].

2.3 Interferometry

Interferometry is an optical measurement technique, which allows the measurement of the relative phase delay of two or more laser beams. Two or more coherent light waves are superimposed that are generally traveling through different distances [21]. The occurring

interference pattern due to the overlay of the laser beams can be analyzed. This reveals information about spatial and temporal distribution in transparent media, its refractive index or changes of the optical path lengths [20].

2.3.1 Phase Difference

The overlay of two laser beams generate an interference pattern which is due to a relative phase difference of the interfering waves. Therefore, the wave properties of light can be used, where the electric field can be written as

$$E = a\cos[2\pi\nu(t - z/c)], \tag{2.5}$$

with a as the amplitude, ν as frequency and c as the speed of light [23]. In the complex representation it takes the form:

$$E = Re(a\exp(i2\pi\nu(t - (z/c))), \tag{2.6}$$

where $Re\{\}$ gives the real part of the expression. The equation can be rewritten with a spatial and temporal varying product:

$$\begin{aligned} E &= Re\{a\exp(-i2\pi\nu z/c)\exp(i2\pi\nu t)\} \\ &= Re\{a\exp(-i\phi)\exp(i2\pi\nu t)\}, \end{aligned} \tag{2.7}$$

with

$$\begin{aligned} \phi &= 2\pi\nu z/c \\ &= 2\pi n z/\lambda, \end{aligned} \tag{2.8}$$

where the traveled optical path is described by the product nz and ϕ as the corresponding phase difference [23]. By taking the real part and assuming that the operations on E are linear, it can be written as:

$$E = A\exp(i2\pi\nu t) \tag{2.9}$$

with

$$A = a\exp(-i\phi) \tag{2.10}$$

as the complex amplitude of vibration [23]. As the frequencies of light waves are extremely high and cannot be measured easily, the distribution of the intensity is taken for optical measurements [20, 23]. The square of the sum of two interfering electric fields is the

intensity:

$$I \approx | \mathbf{E}_1 + \mathbf{E}_2 |^2 \\ = E_1^2 + E_2^2 + E_1 E_2 * cos(\Delta\phi), \tag{2.11}$$

where $\Delta\phi$ is the phase difference which is a result of the optical path difference of the superimposed waves and can be written as

$$\Delta\phi = \frac{2\pi\nu}{c}(n_2 r_2 - n_1 r_1) = \frac{2\pi\nu}{c}(n_2 - n_1)L \tag{2.12}$$

under the condition $r_1 = r_2$ [24]. Constructive interference fringes are occurring for $\Delta\phi = 2\pi n$, where n is an integer and destructive fringes for $\Delta\phi = 2\pi(n+1)$ [25].

2.3.2 Interferometers

For measuring phase difference, various interferometers have been developed. The Michelson Interferometer (Fig.2.5), invented 1887 by Albert Abraham Michelson, is one of the most well known interferometers and is used for example, for measuring linear expansion of transparent materials.

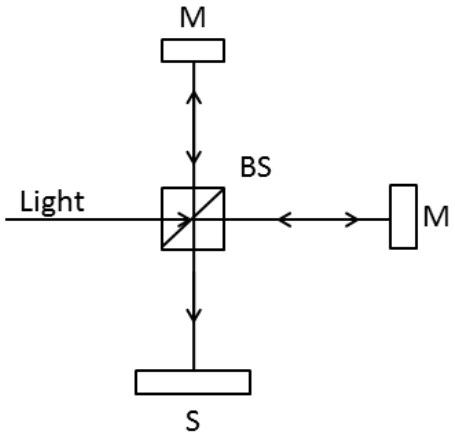

Figure 2.5: Michelson Interferometer. The incident light is splitted into two beams at the beam splitter (BS). These beams travel through the two independent arms of the interferometer and are reflected back by the mirrors towards the beam splitter, where they recombine and travel together until they reach the screen (S). The object under investigation is placed in one of the optical arms.

Another interferometer is the Mach-Zehnder Interferometer (MZI) (Fig.2.6), which was invented by Ludwig Zehnder and Ludwig Mach in 1891. It finds applications in measuring distances, surfaces, velocities and densities [25].

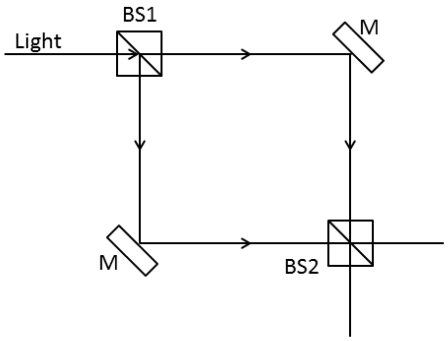

Figure 2.6: Mach-Zehnder Interferometer. The incident light is splitted into two beams at the beam splitter (BS1) and are recombined in beam splitter (BS2). The object under investigation is placed in one of the optical arms in between. The interference pattern can be taken at either of both outputs of the beam splitter.

Within this Master thesis, the Mach-Zehnder interferometer is used because it is sensitive for measuring small phase changes, which arise due to the object under investigation. These phase changes are measured by the occurring interference fringes. For observing the difference of phase due to the object under investigation the interferometer needs to have a fixed linear phase difference as a reference phase. Therefore, the interference in the Mach-Zehnder interferometer needs to be noncollinear, which means that the beams are recombined under an angle within the beam splitter as shown in Fig.2.7 [25].

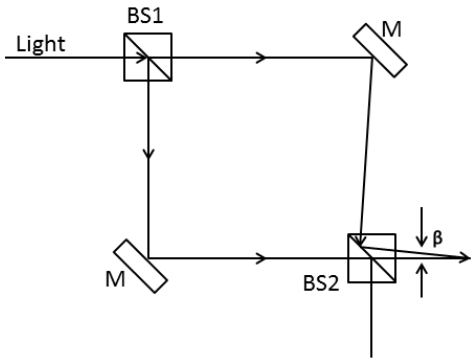

Figure 2.7: Noncollinear Mach-Zehnder Interferometer. The incident light is splitted into two beams at the beam splitter (BS1) and travel two different optical paths until they are recombined under an angle in the second beam splitter (BS2). The object under investigation is placed in one of the optical arms.

When no object is in the beam paths, the occurring interference fringes are a set of vertical lines. As the distance between the line is $\lambda / \sin\beta$, the fringe density increases when the angle increases [25]. The spatial resolution is dependent on the half width d of

one fringe. This width can be calculated:

$$d = \frac{\lambda}{2\tan\beta/2} \tag{2.13}$$

where β is the angle between the beams shown in Fig.2.7. If this width is too small, the fringes are not resolved on the camera screen and if they are too big, the sensitivity of the interferometer decreases [26]. For obtaining the spatial distribution of the object the fringes needs to be analyzed, which is explained in the following section.

2.3.3 Fourier-Transform Phase-Shifting Interferometry

The fringes after the interferometer are detected on a CCD camera and displayed on a monitor. Since the intensity of the fringes in the plane of the detector array is alternating between zero and high values in brightness, it can be expressed by a cosine

$$I(x,y,t) = a(x,y) + b(x,y)\cos(\phi(x,y) + \phi_R(x,y)). \tag{2.14}$$

The background illumination is represented by $a(x,y)$, the noise and contrast variations by $b(x,y)$, the phase related to the object under study by $\phi(x,y,)$ and the reference phase by $\phi_R(x,y)$ [27]. For the analysis of the fringes, the Fourier transform phase-shifting interferometry can be taken [28]. The Fourier transform of a cosine is represented by two identical delta functions at $-\omega$ and ω calculated as follows:

$$\begin{aligned}\mathcal{F}(\cos 2\pi\omega_0 t)(\omega) &= \int_{-\infty}^{\infty} e^{-2\pi i\omega t}\left\{\frac{e^{2\pi i\omega_0 t} + e^{-2\pi i\omega_0 t}}{2}\right\}dt \\ &= \frac{1}{2}\int_{-\infty}^{\infty}(e^{-2\pi i(\omega-\omega_0)t} + e^{2\pi i(\omega+\omega_0)t})dt \\ &= \frac{1}{2}(\delta(\omega-\omega_0) + \delta(\omega+\omega_0)).\end{aligned} \tag{2.15}$$

Figure 2.8 shows a cosine function with a background A and its Fourier transform. The background is located in the Fourier transform at zero frequency and represents the average brightness across the image [30].

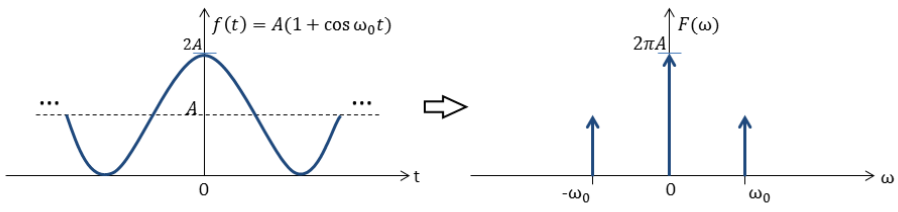

Figure 2.8: Cosine function and its Fourier transform [29].

Figure 2.9 shows the relation of the cosine altering interference fringes picture and its Fourier transform. In the Fourier image, every pixel is a spatial frequency value.

Figure 2.9: Interference fringes shown in a brightness image and its Fourier transform. In the Fourier image, every pixel is a spatial frequency value and the three bright dots in the figure represents the background term in the middle and the mirrored delta function peaks around the background at zero frequency [30].

In the Fourier transform image, there are three bright dots, the central one represents the average background brightness and the left and right peak are identical delta functions mirrored at zero frequency. The Fourier image expresses the brightness of the interference fringes as amplitude of spatial frequency. A back transformation of the Fourier transform gives an exact pixel for pixel copy of the brightness image [30]. Since the central peak represents the background brightness, it does not need to be considered and because the right and left peaks are copies of each other it is adequate to just choose the positive or negative frequencies for the analysis of the interference pattern [27, 30]. By just taking the spatial frequency domain and applying the inverse Fourier transform, the new fringe is complex. The resulting phase of the fringes is given by the argument of the inverse Fourier transform:

$$\phi(x,y) = \tan^{-1}\left\{\frac{\Im(\mathcal{F}^{-1}\mathcal{F}(\omega_0))}{\Re(\mathcal{F}^{-1}\mathcal{F}(\omega_0))}\right\} \tag{2.16}$$

2.3.4 Phase Unwrapping

One more mathematical operation is needed to calculate the phase $\phi(x,y)$. Since the phase is a result of a $\tan^{-1}$, it is defined only over a limited range of angles between $-\pi/2$ and $\pi/2$ [31]. This means that the measured phase is a wrapped version of the true phase by modulo 2π which leads to artificial phase jumps near the boundaries [32]. The discontinuities in the wrapped phase need to be removed to obtain the true continuous phase; this procedure is called phase unwrapping [33]. The basic principle of the phase

unwrapping is that whenever a large discontinuity occurs in the construction, 2π or a multiple of 2π is added to obtain a continuous phase.

$$\phi_{unwrapped}(i) = \phi_{wrapped} + p(i)2\pi, \tag{2.17}$$

where $p(i)$ is an unknown function. The aim of the unwrapping itself is to determine this unknown function [31]. Therefore the phase differences along the path i are examined, where i is the pixel index. The difference of the phase from two neighboring phases is calculated in Eq. 2.18, where $(i-1)$ corresponds to the pixel index of the previous phase to i [31].

$$\Delta\phi_{wrapped}(i) = \phi_{wrapped}(i) - \phi_{unwrapped}(i-1) \tag{2.18}$$

The distance of the fringes determines the difference in the wavefront phase. By having at least two pixels per fringe, the wavefront phase does not change more than π per pixel, which gives a criteria for the reconstruction. Once the phase change from one pixel to the next is larger than π, 2π or a multiple of 2π has to be added or subtracted from the calculated value of the second pixel until the change is again below π [31, 32]. Figure 2.10 shows the basic principle of the phase unwrapping. This method cannot be used for investigating objects that produce a very sharp change in density where the phase change is larger than 2π but since the phase change due to the plume is small, this method can be used for the analysis.

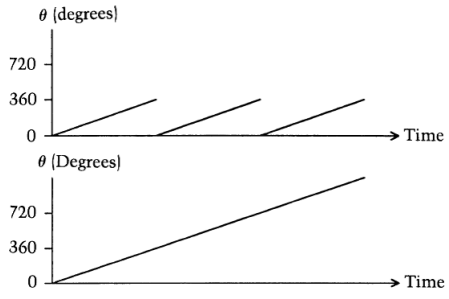

Figure 2.10: Scheme of phase unwrapping. The above graph shows a wrapped phase in degrees over time, where the phase is alternating between 0 and 360 °. The lower graph shows the unwrapped phase, where the phase is continuously increasing [34].

2.3.5 Abel Inversion

The collected interference pattern at the CCD camera is integrated over the line of sight. To get the density distribution along that path, the inverse Abel Transform can be taken. Therefore, the measured vertical distribution needs to be axially symmetric [35].
When a three-dimensional object, described by the function $f(r, \phi, \theta)$, is observed, a two-dimensional projection $h(x, y, z)$ is obtained. The problem now is to calculate the

distribution f out of the projection h [36]. By taking cylindrical coordinates and a distribution perpendicular to the symmetry axis z, which means that z is constant, the relation of projection $h(y)$ and distribution $f(r)$ is given shown in Fig. 2.11.

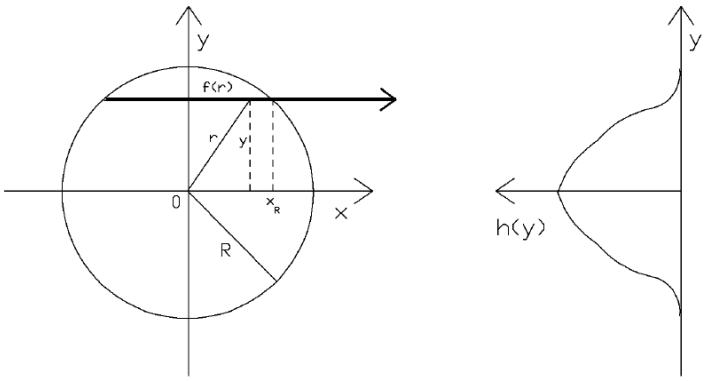

Figure 2.11: Geometrical relation between radial distribution $f(r)$ and vertical distribution $h(y)$ [36].

The mathematical relation can be derived from the geometrical relation from Fig. 2.11:

$$h(y) = 2\int_0^{x_R} dx f(r(x)). \tag{2.19}$$

The substitution

$$dx = \frac{rdr}{\sqrt{r^2 - y^2}} \tag{2.20}$$

follows out of $x^2 + y^2 = r^2$ [24, 36]. By combining Eqs. 2.19 and 2.20 the final distribution follows [35, 36]:

$$h(y) = 2\int_y^{\infty} \frac{f(r)r}{\sqrt{r^2 - y^2}} dr. \tag{2.21}$$

The reconstruction of the distribution can be performed by an inverse Abel transformation:

$$f(r) = -\frac{1}{\pi}\int_r^{\infty} \frac{dF(y)}{dy}\frac{1}{\sqrt{y^2 - r^2}} dy. \tag{2.22}$$

However, the vertical distribution $h(y)$ is not a known analytically described function but consists of the experimentally measured data points. Therefore, the differentiation from Eq. 2.22 cannot be performed. To solve that problem, various methods have been developed [35, 36].
Within this chapter just the Fourier method, developed by Pretzler et. al. [37], will be introduced, which has been used for the analysis. This method is not interpolating the

distribution $f(r)$ and the projection $h(y)$ into subintervals from the border recursively to the center. As a result errors which occur at the border are not taken into account for the calculation of the center of the distribution $f(r)$ [36, 37].
To interpolate the distribution $f(r)$ in one piece, it will be expanded in a series which is similar to a Fourier-series with unknown amplitudes A_n:

$$f(r) = \sum_{n=lF}^{uF} A_n f_n(r) \tag{2.23}$$

where uF represents the upper frequency, lF the lower frequency and $f_n(r)$ is a set of cosine-functions, where

$$f_0(r) = 1$$

and

$$f_n r = 1 - (-1)^n \cos\Big\{n\pi \frac{r}{R}\Big\}. \tag{2.24}$$

Applying this to Eq. 2.21 yields to the Abel transform $H(y)$ of Eq. 2.23.

$$H(y) = 2 \sum_{n=lF}^{uF} A_n \int_y^R f_n(r) \frac{r}{\sqrt{y^2 - r^2}} dr \tag{2.25}$$

with

$$h_n(y) = \int_y^R f_n(r) \frac{r}{\sqrt{y^2 - r^2}} dr. \tag{2.26}$$

These integrals cannot be solved analytically but they can be numerically integrated in advance and stored. Here R belongs to the radius shown in Fig. 2.11. The least-square method determines the unknown amplitudes.

$$\sum_{k=1}^{N} [H(y_k) - h(y_k)]^2 \stackrel{!}{=} min. \tag{2.27}$$

The amount of measured points $y = y_k$ is represented by N, where $h(y_k)$ are the measured data.

$$\begin{aligned} 2 \sum_{n=lF}^{uF} (A_n \sum_{k=1}^{N} h_n(y_k) h_m(y_k)) &= \sum_{k=1}^{N} h(y_k) h_m(y_k), \\ &= \forall m : N_l \leq m < N_u \end{aligned} \tag{2.28}$$

The equation system of 2.28 leads to the Amplitudes A_n, that the distribution $f(r)$ can be calculated. The Fourier based method is derivative free and does not need a pre-treating of the measured data since it is working with an upper frequency limit which acts like a low pass filter [36, 37].

2.3.6 Density Reconstruction

When light propagates through a gaseous transparent medium it changes its phase in comparison to propagation through vacuum. This phase difference is a result of a different refractive index n within the gaseous transparent medium [26]. For calculating the density of the transparent medium, a connection between the refractive index and the gas density needs to be established [38]. Here, we use the Clausius-Mosotti relation

$$\frac{n^2-1}{n^2+2} = \frac{\rho_P}{3}\gamma_{mol}, \tag{2.29}$$

with ρ_P as the particle density (cm^{-3}) and the molecular polarizability of the gas γ_{mol}. The approximation

$$\frac{(n^2-1)}{n^2+1} \approx \frac{2}{3}(n-1) \tag{2.30}$$

leads to

$$n-1 = K\rho_P \tag{2.31}$$

and is the Gladstone-Dale relationship, where K is the Galdstonse-Dale constant [38]. The phase shift corresponds to a projection of the gas density and can be described by a line integral along the optical path [26, 38].

$$\Delta\Phi(y) = \frac{2\pi}{\lambda}\int_y^R \frac{(n(r)-1)r}{\sqrt{r^2-y^2}}dr \tag{2.32}$$

Assuming radial symmetry this refractive index can then be solved by using the inverse Abel transformation

$$n(r)-1 = -\frac{\lambda}{2\pi^2}\int_r^{r0}\frac{d}{dy}(\Delta\Phi(y))\frac{dy}{\sqrt{y^2-r^2}} \tag{2.33}$$

which has been discussed in the previous section. From this relation, the density can be calculated with Eq.2.31. The result of the Abel-inversion is in the unit 1/pixel. It therefore needs to be converted to (particles/cm^3) in order to receive the density, wherefore the scaling factor S can be used.

$$S = \frac{1}{\xi K}, \tag{2.34}$$

where ξ is the scale of the acquired image in µm/pixel [24, 26, 38].

3 Interferometric Measurements

To get a deeper insight in the spatial distribution of the plume, a Mach-Zehnder interferometer was set up and an analysis code was developed to determines small phase changes which provide information about the spatial distribution of the plume. For a time resolved measurement of the plume expansion a pump-probe experiment has been established, where the PIRL acts as the pump and creates the plume by being focused downwards to a water droplet surface. To image the plume, an interferometer with a microchip laser has been set up to work as the probe. For the review of the interferometer and its self-written analysis code, tests runs with a know sample were performed.

3.1 Experimental Setup

For measuring small phase change, a Mach-Zehnder interferometer has been set up.

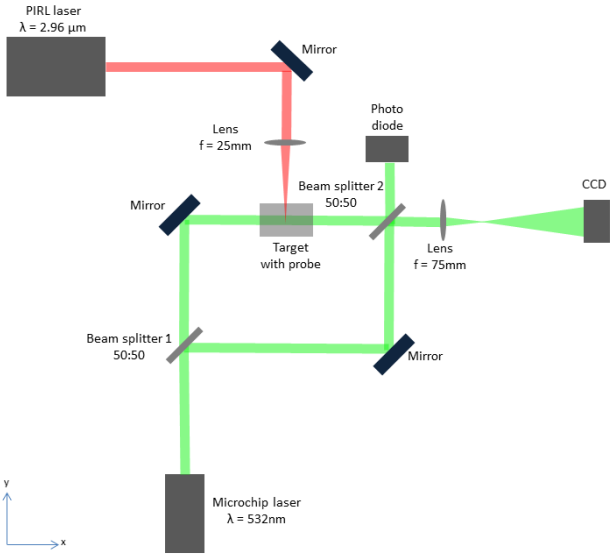

Figure 3.1: Sketch of the MZI. The Mach-Zehnder interferometer consists of two silver mirrors and two beam splitters. The target with the water droplet is placed in one of the interference arms. The beams recombine in the beam splitter 2 under an angle. The plane of the plume is imaged by a lens system onto a CCD camera. For the interferometer, a microchip laser is used (green beam path) and for the ablation, the PIRL is used (red beam path). The photo diode monitors the signal of the microchip laser. For simplicity a collinear MZI is shown.

The Mach-Zehnder interferometer consist out of two 1" non polarizing 50:50 beam splitter cubes and two 1" silver mirrors, which are perpendicularly aligned. The target with the water droplet is placed on a vertical translation stage within one interference arm. The lens, with a focal length of f = 75 mm, is used for imaging the plume onto the CCD camera. Since the splitted beams are recombined in beam splitter 2 under an angle interference fringes occur, which are also displayed and magnified due to the lens on the CCD. The half fringe size in this set up is 2 pixel and determines the spatial resolution to be 3 µm. The microchip laser FDSS 532-Q by CryLaS is used for the interferometry, which has a wavelength of $\lambda = 532$ nm and a pulse energy of 50 µJ, a repetition rate of 1 kHz and a pulse width of $\Delta t = 1.5$ ns and a jitter of 2 ns. The laser can be triggered by an external steerable shutter, which is necessary for the time resolution which will be explained in section 3.3. The photo diode takes a signal whenever the microchip laser pulse travel trough the interferometer.
For the ablation, the PIRL laser is vertically focused downwards onto the surface of the water droplet. Figure 3.2 shows a side view sketch of the target. The arising plume can be investigated by the interferometric measurement with the plume being located in one of the interference arms. The occurring interference fringes are images onto the triggerable CCD camera DMK 23U274 by The Imaging Source.

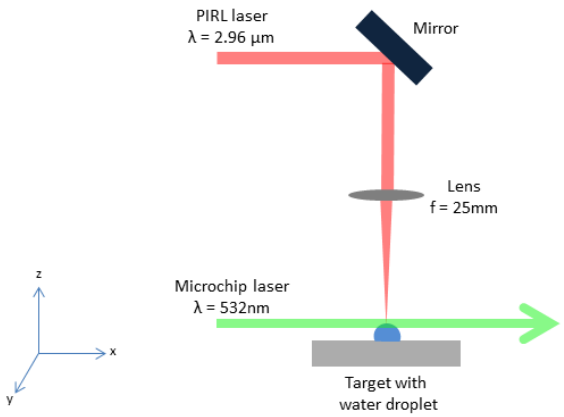

Figure 3.2: Side view of target. The PIRL is focused downwards onto the surface of the water droplet. The occurring plume rises on top of the droplet. The microchip laser pulse travels through the plume. Since the beam diameter of the microchip laser is larger than the width of the plume, the whole distortion due to the plume is in the laser beam of the microchip laser. To increase the contrast of the phase difference, the microchip laser pulse also travels through a part of the water droplet. The microchip laser recombines under an angle afterwards with its reference beam in beam splitter 2 and the interference fringes are imaged on the CCD.

3.2 Trial Experiment of Interferometer and Analysis Code

In order to test the interferometer and the developed code for data analysis, the phase difference induced by lenses was investigated. For that, lenses with different focal lengths were located in one interference arm instead of the ablation plume. The PIRL laser was not needed for this proof of concept since no ablation was required.
In order to obtain the accumulated phase difference, due to the lenses, the interference pattern need was analyzed. As written in section 2.3, a reference interference is taken, to obtained a phase difference as a deformation of the interference fringes. The interference pattern of the reference is shown in Fig. 3.3 and the interference pattern with a lens in the Fig. 3.4.

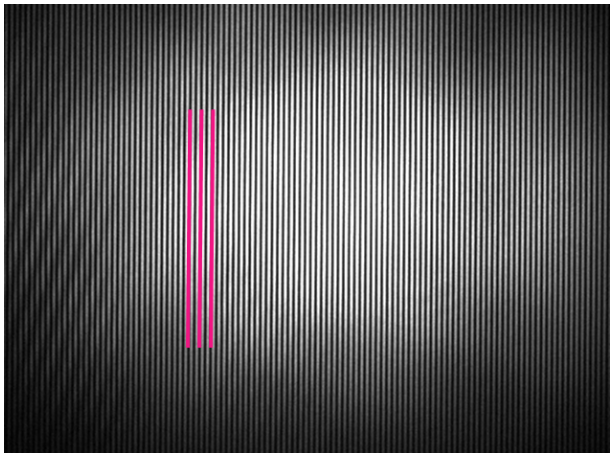

Figure 3.3: Interference pattern of reference. The straight pink marked vertical fringes are the set fringes due to the overlay of the two laser beam within the interferometer. The other visible patterns occur due to noise within each laser beam.

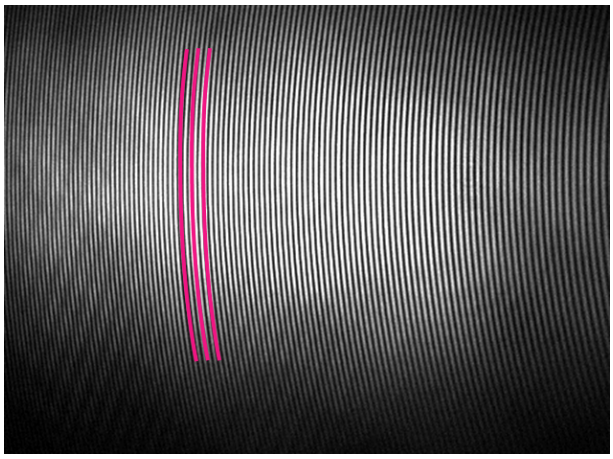

Figure 3.4: Interference pattern of a lens in one arm. The pink marked fringes are slightly curved due to the phase difference the lens is inducing. The pink marked fringes are the fringes of interest. The other visible patterns occur due to noise within each laser beam.

The difference between interferences of the reference and the lens are distinctive. The next step for the calculation of each phase, as written in section 2.3.3 is the Fast Fourier Transform (FFT), which is shown in Fig. 3.5 for the inference of the reference and in Fig. 3.6 of the lens. For the whole analysis of the interference data, a self-written MATLAB code has been used, which is included in the appendix.

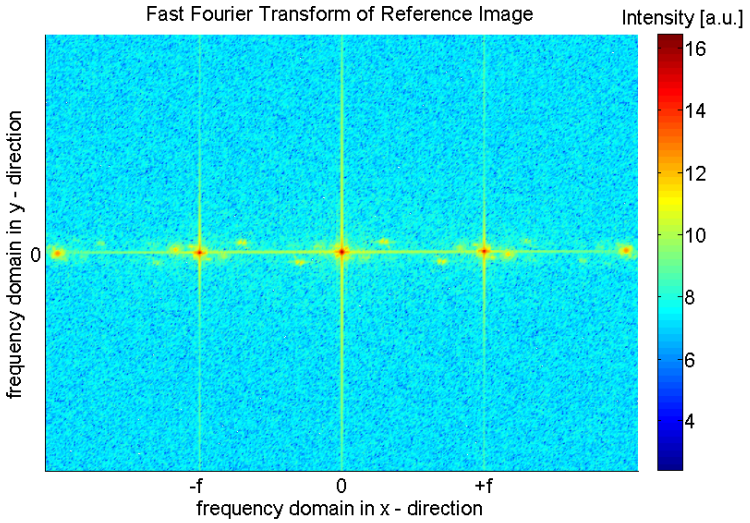

Figure 3.5: Logarithmic plot of Fast Fourier Transform of reference interference. The three peaks occur as explained in section 2.3.3 due to the adjusted phase difference. The other patterns originate from noise within the fringe pattern.

The FFT of a horizontal alternating interference pattern is composed of three horizontally aligned peaks, where the central one describes the background intensity of the interference pattern and the side mirrored peaks are showing either the positive or the negative frequencies of the FFT. Other patterns of the FFT are due to noise within the interference pattern.

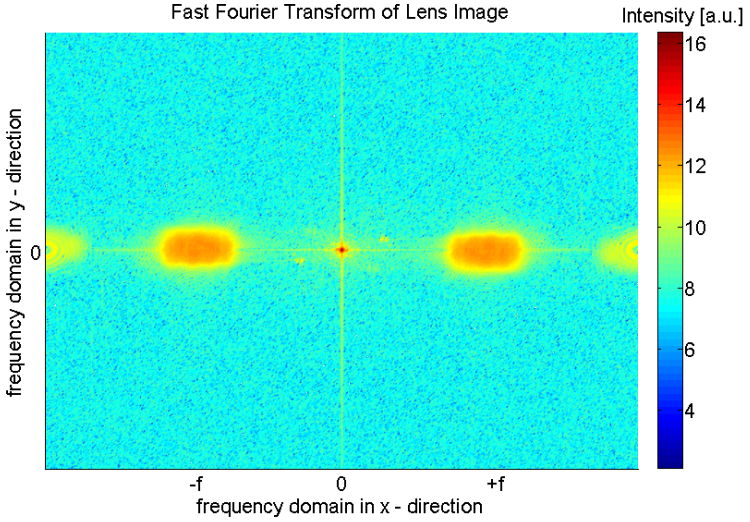

Figure 3.6: Logarithmic plot of Fast Fourier Transform of lens interference.

In the FFT of the lens interference, the mirrored peaks differ from the sharp peaks of the FFT of the reference. This change is due to the deformation of the fringes produced by the lens. Before back transformation, only one frequency component needs to be kept by a bandpass filter, which sets all other intensities to zero. By choosing the right peak, the positive frequency components are kept by the filter or choosing the left peak, the negative frequencies are kept by the filter. Thereby, the bandpass filter needs to be chosen such that much information is kept while keeping the noise low. Figure 3.7 shows the bandpass filtered FFT of the interference pattern and Fig. 3.8 shows the bandpass filtered FFT of the lens interference.

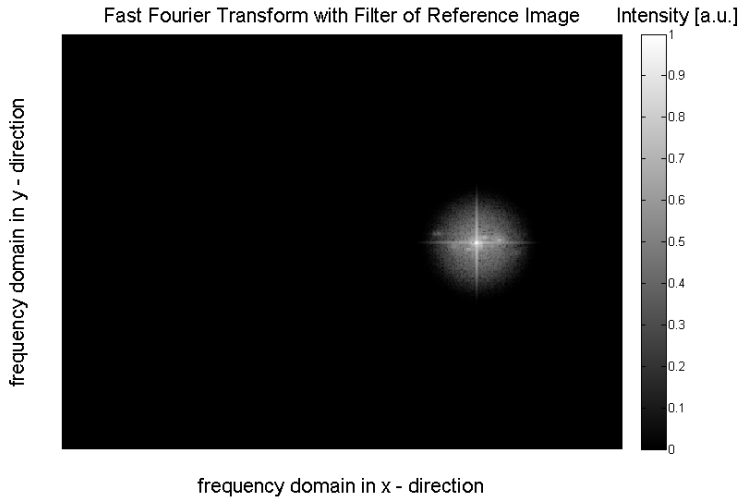

Figure 3.7: Logarithmic plot Fast Fourier Transform with bandpass filter of reference interference.

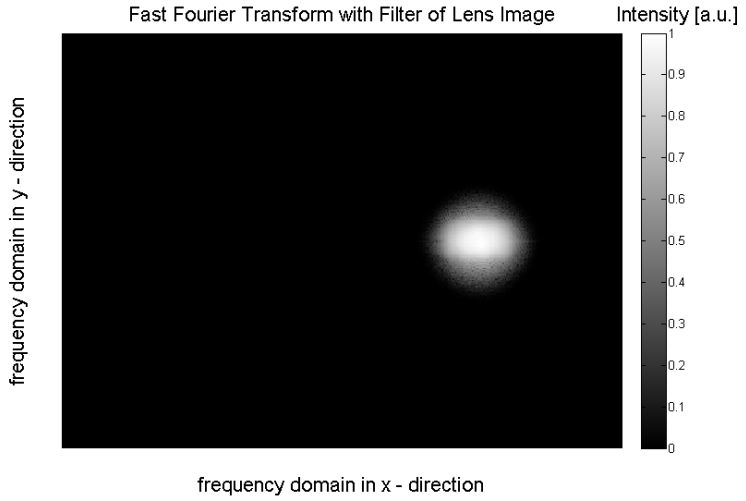

Figure 3.8: Logarithmic plot of Fast Fourier Transform with bandpass filter of lens interference.

After bandpass filtering, the FFT is back transformed to calculate the phase of the interference pattern, as explained in section 2.3.3. Since the result is an alternating phase

between 0 and 2π, the phase needs to be unwrapped, which is shown for the phase of the reference in Fig. 3.9 and of the lens interference phase in Fig. 3.10

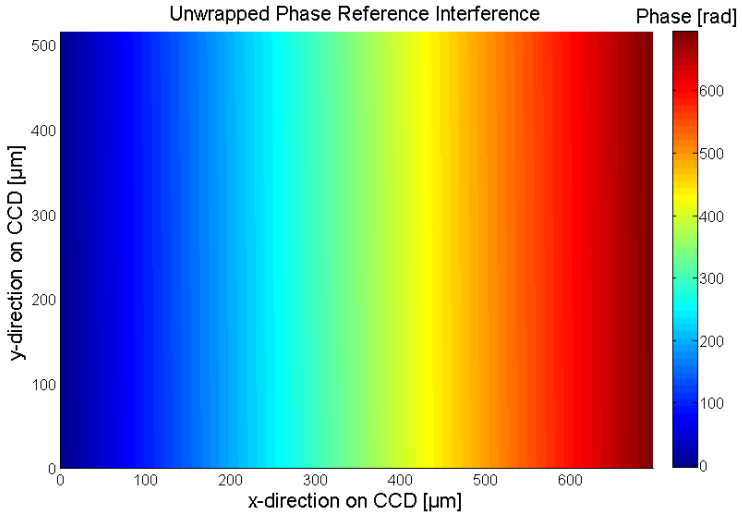

Figure 3.9: Unwrapped phase of reference interference.

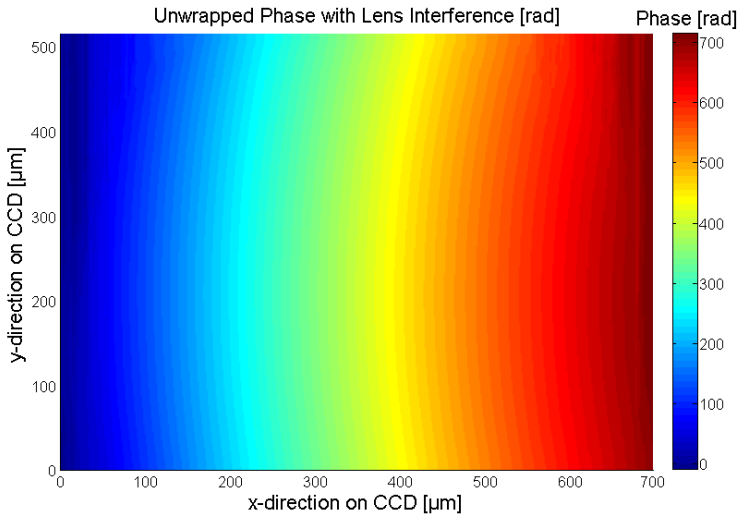

Figure 3.10: Unwrapped phase of lens interference.

The reference phase is a constantly increasing phase, while the lens phase shows a curved formed increasing phase. The last step for calculating the phase difference, which is introduced by the lens, is to subtract the reference phase from the lens interference phase, shown in Fig. 3.11.

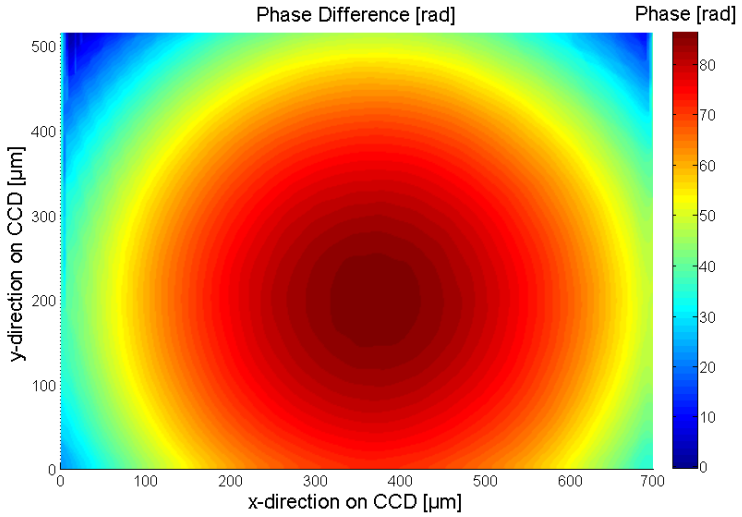

Figure 3.11: Phase Difference of the reference interference phase and the lens interference.

Figure 3.11 shows the phase difference between the two unwrapped phases. The phase shifting interferometry allows to obtain the focal length of a lens f_L [39, 40], since the partial derivative of the object phase $\Phi(x, y)$ is given by

$$\frac{\partial \Phi(x,y)}{\partial x} = \frac{2\pi x}{\lambda f_L}. \tag{3.1}$$

To verify the functionality of the interferometer and the analysis code, two different lenses have been investigated. The calculated focal length out of the slope of the phase difference is shown in Tab. 3.1.

f_t [mm]	f_L[mm]	deviation[%]
125	129	3
150	159	6

Table 3.1: Focal length f_t of the tested lens and the calculated focal length f_L obtained using the interferometer

Since the deviations from the real focal length of the lenses are small, it can be assumed that the interferometer and the analysis code are working correct.

3.3 Time Resolution

In order to investigate the dynamics of the plume expansion, the plume needs to be imaged at different times after formation. Therefore it is necessary to set a fixed delay between the PIRL, which is generating the plume, and the probing microchip laser. A fast shutter within the PIRL setup allows to pick single pulses from the laser system. In this way the repetition rate of the pump probe experiment can be controlled. Figure 3.12 shows a sketch of the timing.

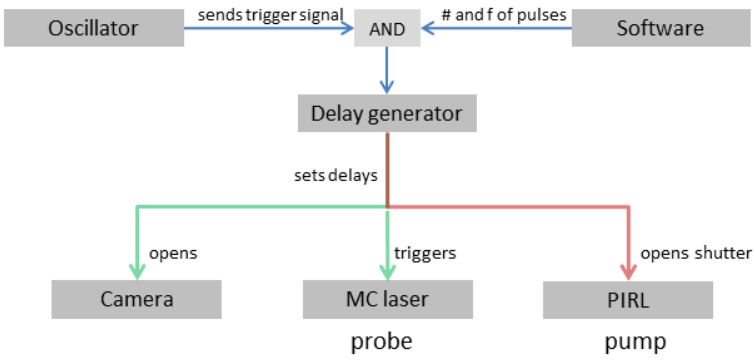

Figure 3.12: Scheme of the timing of the microchip laser (MC) and the CCD camera of the interferometer in relation to the PIRL pulse. The external trigger output of the PIRL seed laser and a software-controlled signal enter an AND gate, whose output triggers the delay generator. The software controls if the delay generator shall send pulses. With the delay generator specific delay times between pulses are set. The green pulse triggers the microchip laser and opens the interferometer camera. The red pulse opens the shutter which lets PIRL pulses pass.

To open the shutter and set a time delay between the PIRL and the microchip laser a delay generator is used. This delay generator is externally triggered by the seed of the PIRL. But to generate the delays, the delay generator also has to get a signal from software, where the amount of the PIRL pulses and its frequency are set. The oscillator of the PIRL and the software are working as an AND gate. If this is fulfilled the delay between the pulse which is opening the shutter and the pulse, which is triggering the microchip laser and opening the camera can be set. It also needs to take into account that the microchip laser still needs time to generate the pulse, which then goes into the interferometer. Therefore the photo diode within the interferometer setup is used to record the MC laser signal. This signal is displayed on an oscilloscope. To obtain the time difference of the PIRL pulse and the microchip laser pulse, the PIRL pulse also is displayed on the oscilloscope. The PIRL pulse is recorded by a photo diode, which is located within the PIRL setup. The recorded PIRL pulse on the oscilloscope is not

the trigger pulse. The trigger pulse, taken from the seed of the PIRL, enables the chain reaction of opening the shutter and camera and triggering the MC laser, that the PIRL pulse after the trigger pulse travels through the shutter and creates the plume.

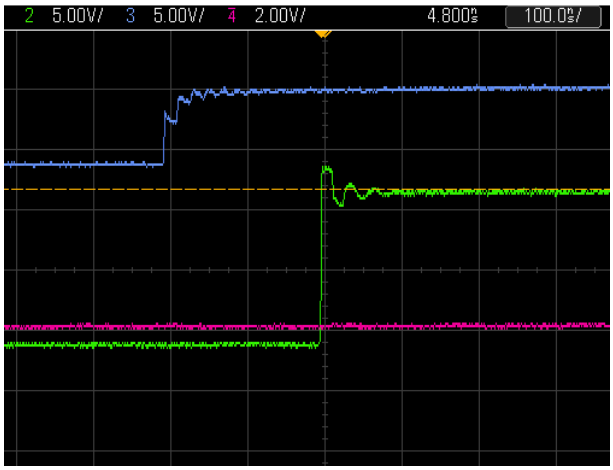

Figure 3.13: PIRL and microchip laser pulses displayed at oscilloscope. The green signal represents the microchip laser pulse, the blue signal the PIRL pulse. The yellow line indicates the trigger. The time scale is 100 ns/unit.

Since the PIRL seed has a jitter of 50 ns, the time difference needs to be measured with the oscilloscope for each shot. The temporal resolution is dependent on the pulse length of the microchip laser, which is 1.5 ns. Therefore, the recorded interference fringe images at the CCD are a snapshot of the plume at a certain delay averaged over 1.5 ns.

3.4 Plume Investigation

The used PIRL laser within this thesis is operating at a wavelength of $\lambda = 2{,}96\,\mu m$ with pulse duration of 7 ps, a repetition rate of 1kHz and a power at ablation of $P = 17\,mW$. For creating the plume, the PIRL is focused by a coated lens with $f = 25\,mm$ downwards to a spot size of $A_f = 1.04 * 10^{-4}\,cm^2$ and a diameter of $D = 130\,\mu m$.
Due to a fixed delay in the microchip laser to match the PIRL pulse, each time a plume arises it is captured by the microchip laser beam and shown in the interference pattern. Here, the temporal resolution is determined by the pulse length of the microchip laser, which is 1.5 ns. As described in section 2.3.2 a static interference is aligned as a reference phase. The phase difference effected by the plume is imaged as a deformation of the interference fringes of the reference. The reference fringe pattern is shown in Fig. 3.14 and the fringe deformation due to the plume in Fig.3.15.

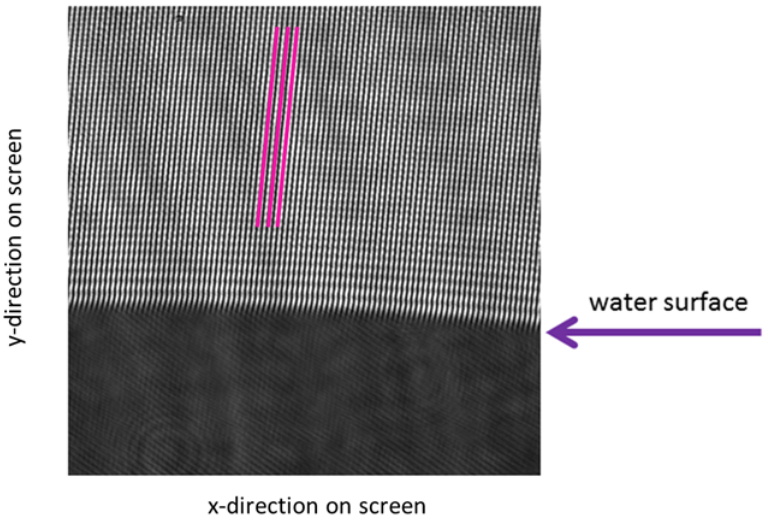

Figure 3.14: Reference interference pattern (indicated by pink lines). The surface of the water droplet is shown as the dark area on the bottom. The water droplet is imaged as a shadowgram by the lens behind beam splitter 2 onto the CCD camera. The lens also magnifies the interference fringes. The interference fringes at the water droplet on the lower part of the image occur due to background interference within the reference beam path and are therefore considered to be noise.

Due to noise within each laser beam, Fig. 3.14 does not only show the slightly diagonal horizontally alternating interference fringes which are aligned by the overlay of the beams within the interferometer. The lens after beam splitter 2 (Fig. 3.1) also images the surface of the water droplet onto the CCD, which is shown as a shadowgram, indicated by the dark area at the bottom of Fig. 3.14. The most noise is filtered out within the data analysis so that it does not affect the results.

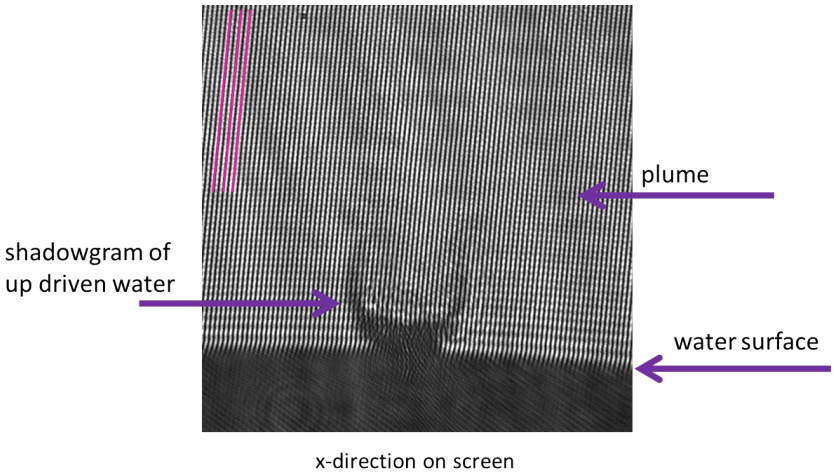

Figure 3.15: Interference pattern with plume. The water surface is shown by the dark area at the bottom. The fringes of the reference interference are still displayed (indicated by pink lines). The plume is on top of the water surface, where the plume front (indicated by the arrow as plume) can be detected as a narrow curve, which is slightly brighter that the fringes. The up driven water is imaged as a shadowgram by the lens after beam splitter 2 onto the CCD. The lens magnifies the interference fringes. The interference fringes at the water droplet on the lower part of the image occur due to background interference within the reference beam path and are therefore considered to be noise.

In order to receive the phase difference, each phase needs to be calculated. As explained in section 2.3.3, firstly the Fast Fourier Transform (FFT) needs to be performed which is shown in Fig. 3.16 for the reference interference and in Fig. 3.17 for the lens interference.

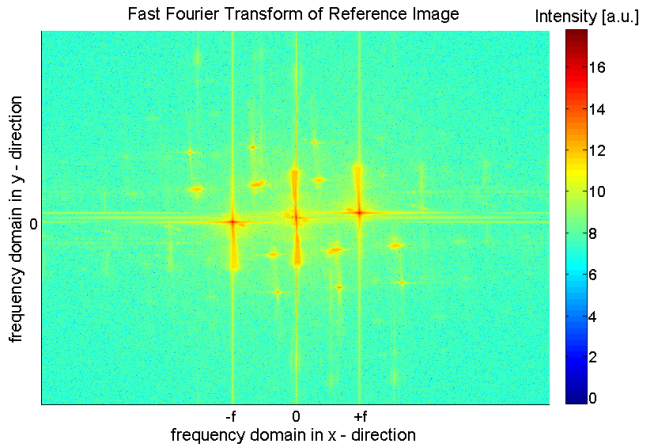

Figure 3.16: Logarithmic plot of the Fast Fourier Transform of the reference image.

The FFT of horizontally alternating interference fringes is, as explained in section 2.3.3, represented by three peaks. The central one represents the background intensity and the two mirrored peaks correspond to the negative and the positive frequency components. Since the reference interference pattern is not exactly horizontally alternating but slightly diagonal, the delta peaks in the FFT are also slightly diagonal. The vertical lines at

the peaks are due to a vertical alternating interference pattern which occurred in one interference arm due to reflection at the water surface. So they do not belong to the interference of the MZI and can be seen as noise. In addition, the diagonal symmetrical arranged dots close to the interference peaks are background noise. This noise is reduced by keeping the positive frequency peak by applying a filter before back transformation, which is the next step of the analysis.

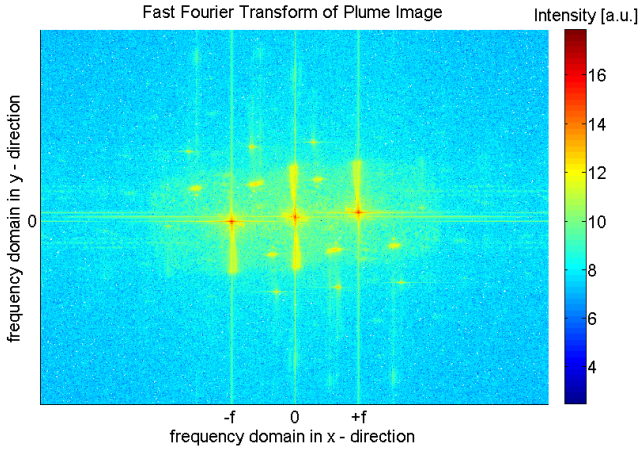

Figure 3.17: Logarithmic plot of the Fast Fourier Transform of the plume image.

The FFT of the interference with the plume shown in Fig. 3.17 differs from the FFT of the reference interference FFT in Fig. 3.16. For calculating the phase only the positive frequencies of the FFT are considered. Since the phase information is also around the peak, the filter has to be adjusted such that enough information is selected while keeping the noise low. Figure 3.18 shows the FFT of the plume interference with an ellipsoid Gaussian bandpass filter.

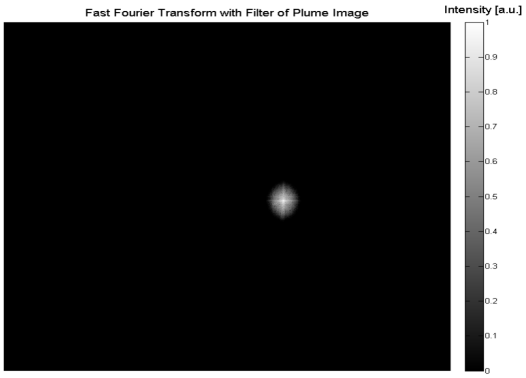

Figure 3.18: FFT of plume with bandpass filter

After bandpass filtering, the FFT needs to be back transformed for the phase calculation. As explained in section 2.3.3, the phase is alternating between 0 and 2π. Therefore, it needs to be unwrapped, which is shown in Fig. 3.19 for the reference phase and in Fig. 3.20 for the plume phase.

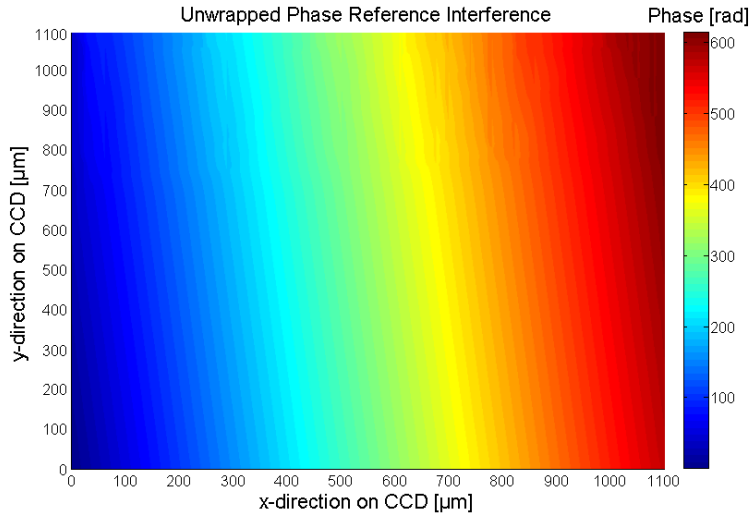

Figure 3.19: Unwrapped phase of the reference interference

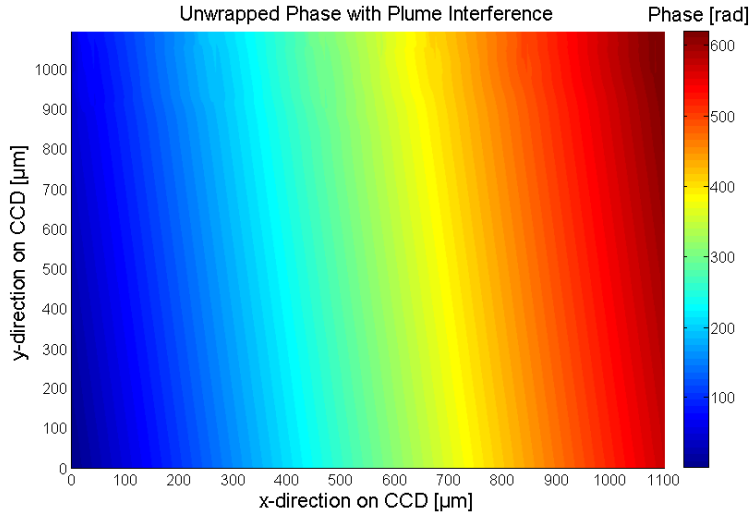

Figure 3.20: Unwrapped phase of the plume interference

A difference between these phase maps is not as obvious as it was for the interference with a lens because the phase difference due to the plume is very small. The phase difference is shown in the following section.

3.5 Results

Within this section the results of the interferometric measurements and analysis are presented.

3.5.1 Phase Difference

Figure 3.21 shows the phase difference of an interference with a plume at $\Delta t = 450\,ns$, where Δt describes the time delay between the PIRL pulse which is creating the plume and the microchip laser pulse that creates the interference pattern.

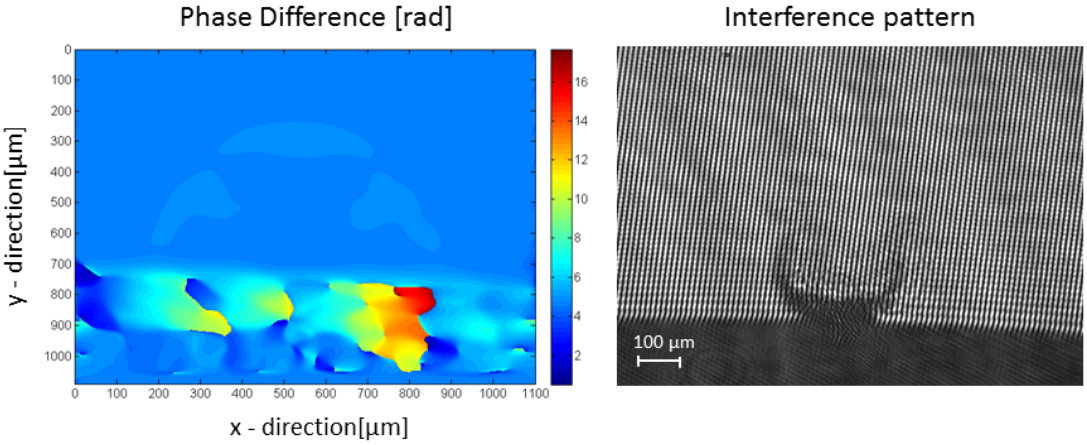

Figure 3.21: Phase difference due to the plume on the left and the interference picture of the plume on the right. The phase map shows phase changes affected by the plume as well as phase changes due to the water surface in the lower part of the phase map. The interference picture shows that the interference pattern is only above the water surface. The laser beam is scattered within the water so that the phase changes on phase map is considered to be noise. The laser pulse duration for the PIRL was 7 ps, wavelength $\lambda = 2.96\,\mu m$, the spot size of $A_f = 1.04 * 10^{-4}\,cm^2$, and the fluence $F = 0.16\ J/cm^2$.

The water droplet scatters mostly all of the microchip laser beam away. Therefore no phase change can be imaged for the water and no fringes occur. Due to background interference within the reference beam in the interferometer, there is an interference pattern below the water surfaces. It was not possible to filter out this background interference within the bandpass filtering since its interference pattern was too close to the phase changes due to the plume within the FFT. Consequently, the phase map shows phase changes at the position of the water, which can be considered as noise. In the interference pattern a lunate shadowgram of upcoming water can be detected, which is not resolved in the phase map. The rising water throws a shadow onto the CCD camera, which darkens the interference pattern so that changes of the fringes cannot be resolved.

Because of that, the phase change due to the arising water is not shown in the FFT close to the frequency wings of the cosine but at another position. During the Fourier filtering this information is cut out. Including it would lead to a weaker contrast of the phase difference due to the plume, which is already small.
Since the plume is the object of investigation, the area of phase change due to the plume can be cut out to receive a higher resolution, shown in Fig. 3.22.

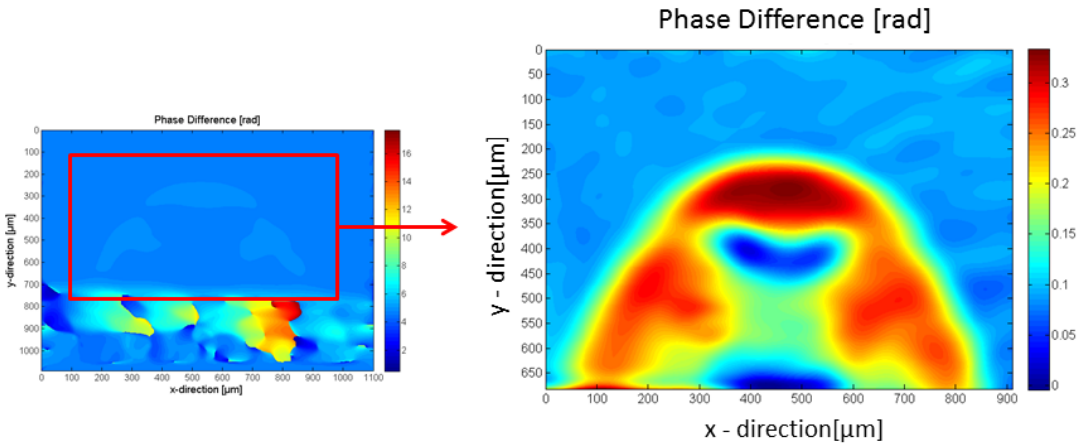

Figure 3.22: Phase difference due to the plume.

The upper blue part with low phase change indicates a large fraction of vapor phase, which is driving a water front to the top, indicated by a larger phase change. In the work of Franjic [8], the less dense region inside the plume is referred to as an air shock wave. The shape and the value of the phase difference due to the plume represents the shape and spatial distribution of the plume.

3.5.2 Plume Expansion Velocity

For estimating the expansion of the plume, the interference was recorded for different time delays between the PIRL laser, which generates the plume, and the microchip laser, which images the interference. Each collected interference pattern shows a different plume because the time delay, displayed on the oscilloscope, needed to be recorded by hand simultaneously to the automatically stored interference pattern. Therefore the PIRL frequency was set to 0.1 Hz. Fig. 3.23 and Fig. 3.24 display the time resolved plume expansion.

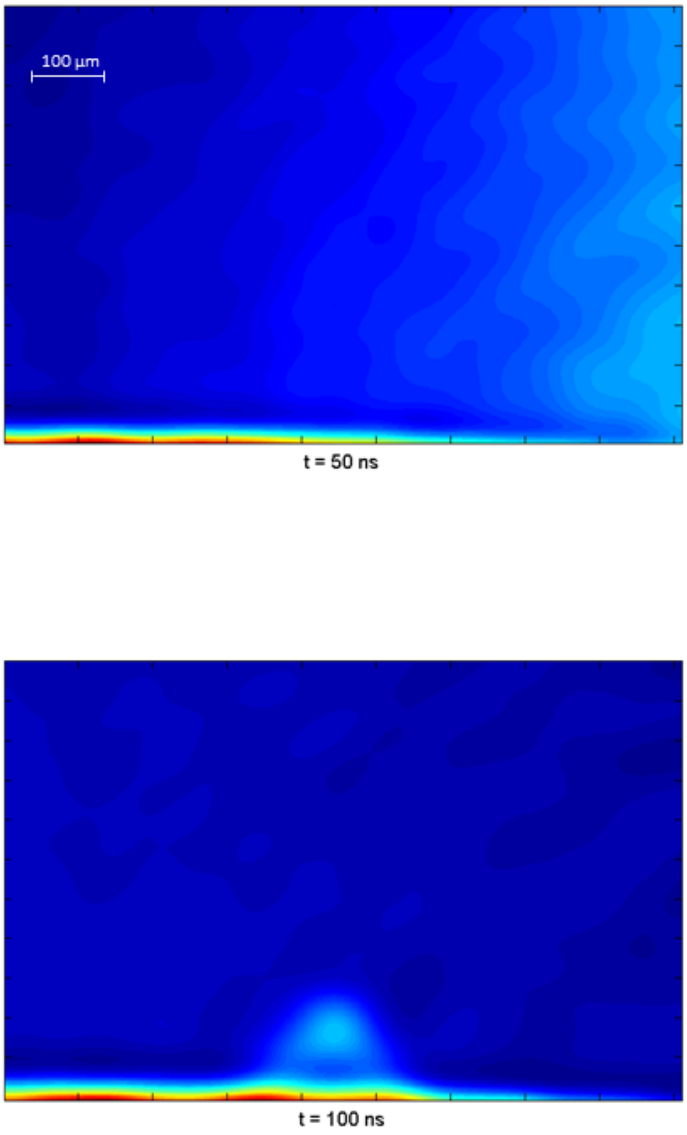

Figure 3.23: Phase difference map of the plume at different delay times. The upper image is taken at $\Delta t = 50\,\text{ns}$, the lower one at $\Delta t = 100\,\text{ns}$. The laser pulse duration was 7 ps, wavelength $\lambda = 2.96\,\mu\text{m}$, spot size $A_f = 1.04^{-4}\,\text{cm}^2$, and a fluence $F = 0.16\,\text{J/cm}^2$. All phase maps are imaged at the same scale.

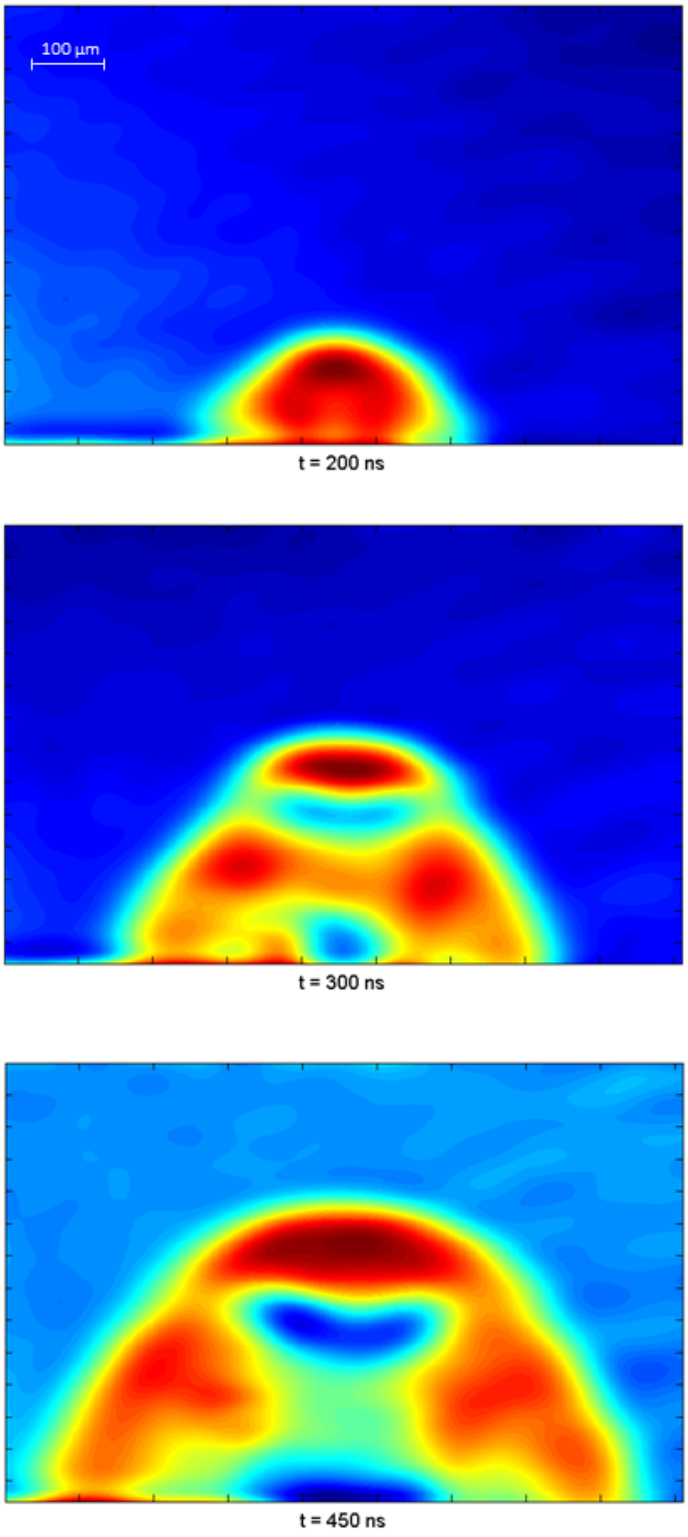

Figure 3.24: Phase difference map of the plume at different delay times. The top image is taken at $\Delta t = 200\,ns$, the middle one at $\Delta t = 300\,ns$ and the lowest one at $\Delta t = 450\,ns$. The laser pulse duration was $7\,ps$, wavelength $\lambda = 2.96\,\mu m$, spot size $A_f = 1.04^{-4}\,cm^2$, and a fluence $F = 0.16\,J/cm^2$. All phase maps are imaged at the same scale.

In order to calculate the velocity of the plume expansion, the plume height was measured for different time delays of the PIRL and the microchip laser pulse. The time delay between PIRL and microchip laser was set at the delay generator. But the seed of the PIRL has a jitter that the delay varies from shot to shot. Therefore, the time delay between PIRL and microchip laser is recorded for each shot. Figure 3.25 shows the top position of the plume as a function of time.

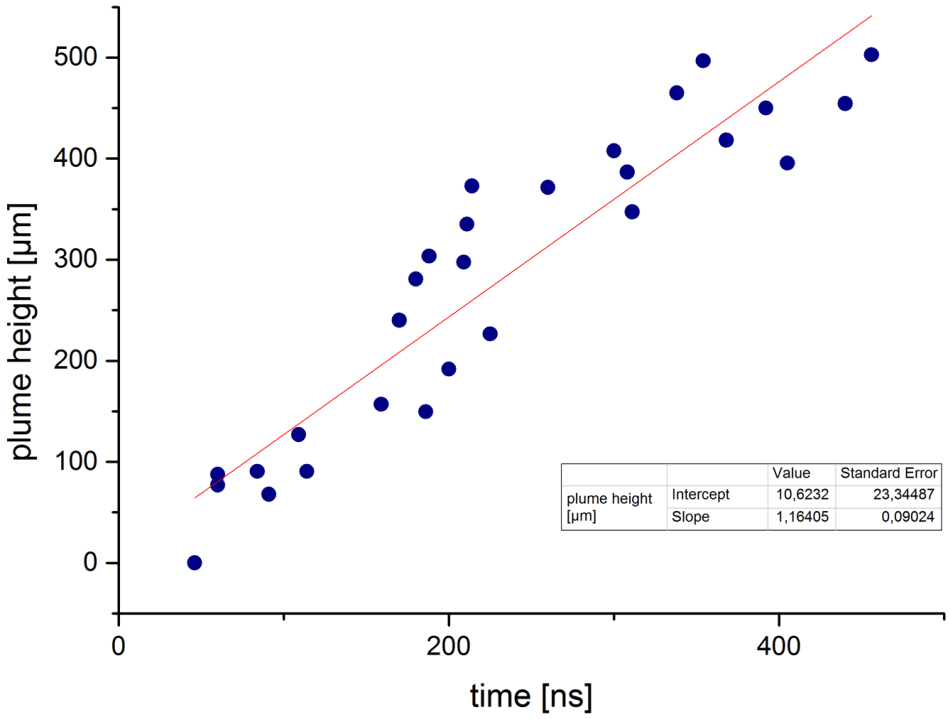

Figure 3.25: Plume top position as a function of time for a laser fluence of $F = 0.16\,J/cm^{-2}$.

Figure 3.25 shows a linear trend and the velocity is calculated as a linear fit of the the data points. At a time delay of 45 ns no plume height was measured because no phase change was detected, which is also shown in Fig 3.23. The average vertical velocity of the plume expansion is $v = 1.16\,km/s$.

4 Discussion and Outlook

Within this thesis, it has been shown that the interferometer setup in tandem with the analysis code can be used to measure the phase difference, which occurs due to the ablation plume created by the PIRL laser. Furthermore, the velocity of the plume expansion has been determined. Comparing the plume shapes of the dark field images measured by Franjic (upper images in Fig. 4.1) [8] with the measured phase-change distribution of the plume (lower images in Fig. 4.1), a clear similarity is observed.
At the upper part of the plume of the dark field image at 184 ns, the reflection of the light is high, following from a narrow low reflection to another high reflection. This double structure can also be detected at the phase map of the spatial distribution at $\Delta t = 450\,ns$ by a high phase change at the top (red area), followed by nearly no phase change (blue area), to a slightly increased phase change (green area). According to Franjic [8], the transparent narrow upper portion of the plume in the dark field image indicates a strong air shock wave, which could correlate to the upper blue region within the phase map at $\Delta t = 450\,ns$.

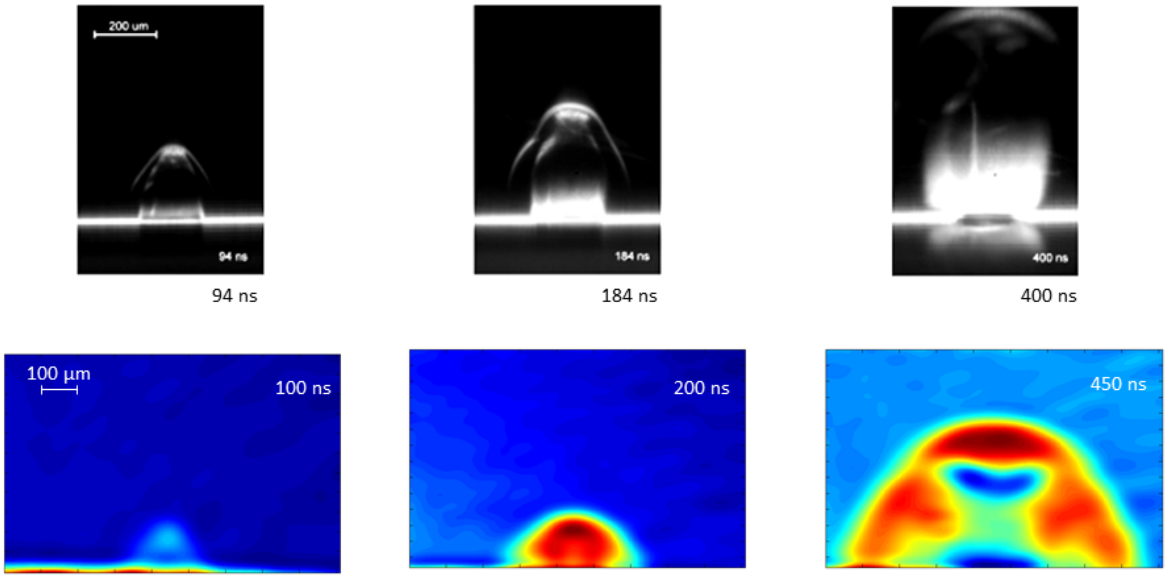

Figure 4.1: Representative time resolved dark-field images of the plume expansion published by Franjic [8] on the upper part at a laser fluence of $0.83\,J/cm^2$. Plume expansion measured within this thesis on the lower part at a laser fluence of $0.16\,J/cm^2$.

Also noticeable is that the shape of the dark field plume after 94 ns matches better with the measured spatial distribution of the plume after 200 ns and the 184 ns dark field with the 450 ns plume distribution. This can be explained by different laser fluences. The dark field images were created from experiments, where the laser fluence was $F = 0.83\,J/cm^2$ whereas the laser fluence for the experiments in the framework of this thesis is $F = 0.16\,J/cm^2$. Consequently, the laser fluence strongly affects the velocity of plume formation.

The calculated vertical expansion velocity and the velocities measured by Franjic [8] are in good agreement, shown in Fig. 4.2. The measured velocity in this thesis is a bit higher than the results of Franjic for the same fluence, which could be an effect of the shorter pulse duration of the used PIRL in this thesis. The PIRL pulse duration for the plume expansion in Franjics experiments is 140 ps whereas the pulse duration of the PIRL in this thesis is 7 ps. The shorter pulse duration enables a faster energy deposition, therefore, a faster plume expansion. The measured plume expansion velocity for a fluence of $F = 0.16\,J/cm^2$ is added as a pink dot to the graph in Fig. 4.2, which displays the velocity as a function of fluence measured by Franjic.

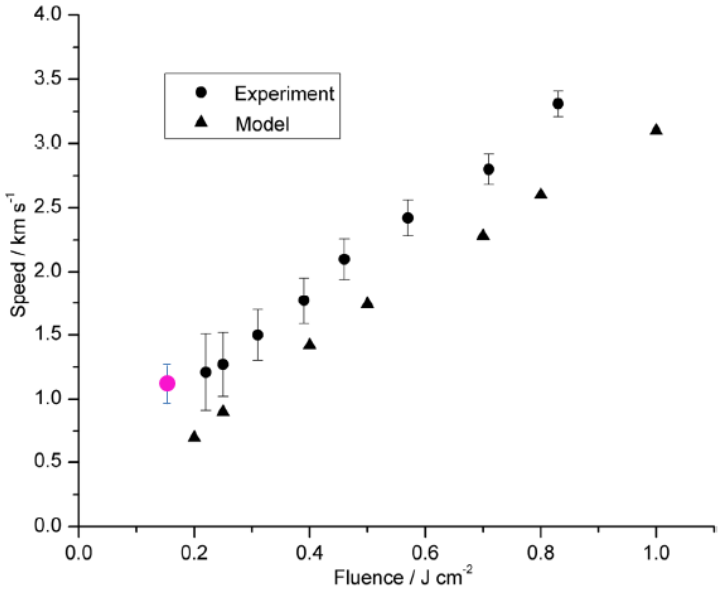

Figure 4.2: Calculated velocity of the plume at fluence $F = 0.16\,J/cm^2$ (pink dot) within the experimental and modeled plume velocities as function of laser fluence. Image taken from Franjic [8].

The advantage of interferometry is its sensitivity. But this sensitivity is limited by the magnitude of random phase fluctuations. For very high precision, which is necessary for resolving small refractive index changes due to the plume, noise needs to be reduced. Disturbances can be caused from mechanical vibrations, air flow, laser pulse intensity fluctuations and temperature fluctuations.

To improve the resolution the setup can be moved into vacuum, with a fixed temperature and a controlled air flow. However, moving the interferometer into vacuum can change the plume dynamics because of the lower air pressure. In order to get the exact density distribution of the plume, the Abel Inversion needs to be performed.

Further measurements with different laser fluences offer more information about the plume dynamics. Moreover, a higher time resolution is achieved by measuring with smaller time difference steps between the PIRL and the microchip laser. Also various samples can be investigated for resolving differences in the plume dynamics. Since the collection of the data within this thesis was laborious and time-consuming, a storage and time delay control unit has been developed to increase the sampling amount in time. This unit combines the control of the shutter, the delay generator and the oscilloscope and collects the interference pattern and the time delay and the pulse energy. Since the energy of each laser pulse varies, the storage and time delay control unit can be used to automatically store each measured pulse energy of the PIRL pulse. The sampling efficiency for the following experiments will be highly increased by the storage unit.

Consequently, the interferometer setup in tandem with the analysis code can be considered to measure the spatial phase-change distribution and determine the velocity of the plume expansion.

5 Appendix

5.1 MATLAB Code

```
%% Deformation within one interence arm
%
%This program finds the true phase of 2 images. Where one image is a
%comparison image with just the normal fringes. The second one is the image
%of the deformation. This program unwrappes their phases and substract them
%from each other to find the true deformation which is caused by the
%destortion in one of the interference arms. Afterwards the program
%performs an Abel Inversion by using the Fourier Method, to get the
%distribution of the projection, which is given by the phase of the
%interferometer.

clc
%% variables that needs to be changed for each image.
clear all
close all

% for the gaussian filter
X =  369;    % these are the coordinates of the peak, which is selected
Y =  455;    % for calculation of the phase
lu = 9;      % the are the boundaries for the width of the Gaussian
lr = 13;     % or an elliptical

%Setup Variables
lambda = 532E-9;              %wavelength
pxl = 4.4E-6;                 %size for each pixel, which the camera resolves
G = 7.67E-36;                 %[cm^3] Gladstone-Dale constant steam
S_ai = lambda\(2*pi*pxl*G);   % scaling factor for able inversion
re = 2.82E-15;                %classical electron radius


%% reading the files
%Image_1 is the reference interference
Image_1 = imread('C:\Users\kstrahl\Pictures\Auswertung\02_12\zeitmessung\1.
set\refa.bmp');
Image_1 = nearest_neighbor(double(rgb2gray(Image_1)));

%Image_2 is the plume interference
Image_2 = imread('C:\Users\kstrahl\Pictures\Auswertung\02_12\zeitmessung\1.
set\Image0016a.bmp');
Image_2 = nearest_neighbor(double(rgb2gray(Image_2)));


%% Image Processing

%Fourier filtering and phase unwrapping
[Phase_Image1,FFTA_1,fFilterA_1,tFilterA_1, amplitude1] =
Image_unwrapping(Image_1, lu, lr, X ,Y, O, U,r);
[Phase_Image2,FFTA_2,fFilterA_2,tFilterA_2, amplitude2] =
Image_unwrapping(Image_2, lu, lr, X ,Y, O, U,r);

UnwrappedPhase = Phase_Image2 - Phase_Image1;
```

```
% Function for filtering


function BPFilter = gaussfilter(A, B, lu, lr, MaxX ,MaxY, O, U,r)

x=linspace(0,B,B);
y=linspace(0,A,A);
[X,Y]=meshgrid(x,y);

coeff = 1/sqrt((2*pi*((lu)/2)^2));

% Gaussian filter
BPFilter = coeff * exp(-(((X-X(MaxX,MaxY)).^2+(Y-Y(MaxX,MaxY)).^2))/...
  (((lu)^2)));

%super Gaussian filter
BPFilter = coeff * exp(-(((X-X(MaxX,MaxY)).^4+(Y-Y(MaxX,MaxY)).^4))/...
  (((lu)^4)));

% elliptycal filter
BPFilter = exp(-((X-X(MaxX,MaxY)).^2/lu^2+(Y-Y(MaxX,MaxY)).^2/lr^2));


BPFilter = BPFilter/max(max((BPFilter)));


end



%% Function for phase unwrapping
function [Phase_Image1,FFTA_1,fFilterA_1,tFilterA_1, amplitude] = Image_unwrapping(ImA, lower_A,
upper_A, A, B, O, U,r)


%% Image Processing

[A1, A2] = size(ImA);

%constructing the filter for selecting the rigth filter
BPFilterA = gaussfilter(A1, A2, lower_A, upper_A, A ,B, O, U,r);
[F1A, F2A] = size(BPFilterA);


%converting the image into frequency domain
FFTA_1 = fftshift(fft2(ImA, F1A, F2A));
fFilterA_1 = BPFilterA.*FFTA_1; %convolution in freq domain


%conversion back into time domain
tFilterA_1 = ifft2(ifftshift(fFilterA_1));
tFilterA_1 = tFilterA_1(1:A1, 1:A2);


%calculating the phase
PhaseA = atan2(imag(tFilterA_1), real(tFilterA_1));


%calculatin the Amplitude
amplitude = sqrt((imag(tFilterA_1)).^2+(real(tFilterA_1)).^2);


%unwrapping all rows at the same time
for i=1:A1
   PhaseA(i,:) = unwrap(PhaseA(i,:));
end
%unwrapping all colums at one time
for i=1:A2
   PhaseA(:,i) = unwrap(PhaseA(:,i));
end


Phase_Image1 = PhaseA;
end
```

Table for graph fig.3.25

Δt [ns]	Δ h [µm]
46	0
60	77
60	88
84	91
91	68
109	127
114	77
159	157
170	240
180	281
186	149
188	304
200	192
209	297
211	335
225	373
214	227
260	371
300	387
308	408
311	347
338	465
354	497
368	418
393	450
405	396
440	454
456	503

Table 5.1: Height of plume for different time delays between PIRL and microchip laser

Bibliography

[1] Franjic K., Cowan M.L., Kraemer D., Miller R.J.D., *Laser selective cutting of biological tissues by impulsove heat deposition through ultrafast vibrational excitations*, Opt Express, Vol. 17, 22937-22959 (2009)

[2] Amini-Nik S.,Kraemer D. ,Cowan M.L., Gunaratne K., Nadesan P., et al., *Ultrafast Mid-IR Laser Scalpel: Protein Signals of the Fundamental Limits to Minimally Invasive Surgery*, PLoS ONE 5(9):e13053. doi:10.1371/journal.pone.0013053

[3] Beer, *Bestimmung der Absorption des roten Lichts in farbigen Flüssigkeiten*, Annalen der Physik und Chemie, Vol. 86, 78-88 (1852)

[4] Niemz M.H., *Laser-Tissue Interactions, Fundamentals and Applications*, Springer-Verlag, Berlin-Heidelberg, 3 (2007)

[5] Kwiatkowski M., Wurlitzer M., Omidi M., Ren L., Kruber S., Nimer R., Robertson W.D., Horst A., Miller R.J.D., Schlüter H., *Ultrafast Extraction of Proteins from Tissues Using Desorption by Impulsive Vibrational Excitation* Angew. Chem. Int. Ed. 54, 285-288 (2015)

[6] Franjic K., University of Toronto (Toronto) (2010)

[7] Vogel A., Venugopalan V., *Mechanisms of Pulsed laser Ablation of Biological Tissues* Chem. Rev. 103, 577-644 (2003)

[8] Franjic K., Miller R.J.D., *Vibrationally excited ultrafast thermodynamic phase transitions at the water/air interface*, Phys. Chem. Chem. Phys., Vol. 12, 5225-5239 (2010)

[9] Cowan M.L., Bruner B.D., Huse N., Dwyer J.R., Chugh B., Nibbering E.T.J. , Elsaesser T and Miller RJD, *Ultrafast memory loss and energy redistribution in the hydrogen bond network of liquid H_2O*, Nature Vol. 434, 199-202 (2005)

[10] K. L. Vodopyanov, *Saturation studies of H2O and intense picosecond laser pulses*, J. Chem. Phys., Vol. 94, 5389–5393 (1991)

[11] Schwarzer D., Lindner J., Vöhringer P., *OH-stretch vibrational relaxation of HOD in liquid to supercritical D2O* , J Phys Chem A., Vol. 110(9), 2858-2867 (2006)

[12] Schäfer T., Lindner J., Vöhringer P., Schwarzer D., *OD stretch vibrational relaxation of HOD in Liquid to supercritical H_2O*, J. Chem.Phys., Vol. 130, 224502 (2009)

[13] Ling R., Robertson W.D., Reimer R., Heinze C., Schneider C., Eggert D., Truschow P., Hansen N.-O., Kroetz P., Zou J. and Miller R.J.D., *Towards instantaneous cellular level bio diagnosis: laser extraction and imaging of biological entities with conserved integrity and activity*, Nanotechnology Vol.26, 284001 (2015)

[14] Müller G., Dörschel K., Kar H., *Biophysics of the Photoablation Process*, Lasers in Medical Science Vol.6, 241 (1991)

[15] Bertie J.E., Lan Z., *Infrared Intensities of Liquids XX: The Intensity of the OH Streching Band of Liquid Water Revisited, and the Best Current Values of the Optical Constants of H2O(I) at 25° C between 15,000 and 1cm^{-1}* , Applied Sectroscopy Vol.50, 1047-1057 (1996)

[16] Hess M., Hildebrandt M.D., Müller F., Kruber S., Krotz P., Schumacher U., Reimer R., Kammal M., Püschel K., Wöllmer W., Miller R.D.J., *Picosecond infrared laser (PIRL): an ideal phonomicrosurgical laser?*, Eur Arch Otorhinolaryngol Vol. 270, 2927-2937, Springer Verlag (2013)

[17] Weiner A.M.,*Ultrafast Optics* , John Wiley& Sons (2009)

[18] Rulliére C., *Femtosecond Laser Pulses*, Springer Verlag (2005)

[19] Cerullo G., De Silvestri S., *Ultrafast optical parametric amplifiers*, Review of Scientific Insturments Vol. 74 No.1 (2003)

[20] Osten W., *Digitale Verarbeitung und Auswertung von Interferenzbildern*, Akademieverlag Berlin (1991)

[21] Donges S., Noll R., *Laser Measurement Technology - Fundamentals and Applications*, Springer Series in Optical Sciences Vol. 188 (2015)

[22] Hugenschmidt M., *Lasermesstechnik - Diagnostik der Kurzzeitphysik*, Springer Verlag(2007)

[23] Hariharan P., *Optical Interferometry*, Elsevier (2003)

[24] Ridder S., *Ortsaufgelöste Messung der Elektronendichte mittels Laser-Interferometrie in einem gepulsten Plasma*, Ruhr-Universität Bochum (2011)

[25] Galvez E.J., *Gaussian Beams*, Colgate University (2009)

[26] Pelka A., *Bestimmung der Elektronendichte in lasererzeugten Plasmen mittels Laserinterferometrie*, Technische Universität Darmstadt (2005)

[27] Lewis A.J. *Absolute length measurement using multiple-wavelength phase-stepping interferometry*, Imperial College London (1994)

[28] Deck L.L., *Fourier-transform phase-shifting interferometry*, Applied Optics, Vol. 42, No.13 (2003)

[29] Hecht E., *Optics* 4th Edition, Addison Wesley (2002)

[30] Lehar S., *An Intuitive Explanation of Fourier Theory* http://cns-alumni.bu.edu/ slehar/fourier/fourier.html (11.12.2015)

[31] Greivenkamp J.E., Bruning J.H., *Phase shifting interferometry*, in Optical Shop Testing, 2nd ed., D. Malacara, Wiley (1992)

[32] Abbas K., *A new recurrent approach for phase unwrapping*, Int. J. Appl. Sci. Eng., Vol.3, 135-143 (2005)

[33] Meneses J., Gharbi T., Humbert P., *Phase-unwrapping algorithm for images with high noise content based on a local histogram*, Applied Optics, Vol.44, No. 7 (2005)

[34] Dolson M., *The Phase Vocoder: A Tutorial*, Computer Music Journal, Vol. 10, No.4, The MIT Press (1986)

[35] Fulge H., Knapp A., Eichhorn C., Wernitz R., Löhle S., Faoulas S., Herdrich G., *Improved Abel Inversion Method for Analysis of Spectral and Photo-Optical Data of Magnetic Influenced Plasma Flows*, AIAA, 3456 (2011)

[36] Thomson M., *Side-On Messungen der Balmerlinie H_α in einem Plasma hoher Dichte* Christian Albrecht Universität Kiel (1994)

[37] Pretzler G., *A New Method for Numerical Abel-Inversion* Z. Naturforsch., Vol. 46 a, 639-641 (1991)

[38] Schmid K., *Supersonic Micro-Jets and Their Application to Few-Cycle Laser-Driven Electron Acceleration*, LMU München (2009)

[39] Tay C.J., Thakur M., *Measurement of focal length of lens using phase shifting Lau phase interferometry*, Optics Communications Vol. 248, 339-345 (2005)

[40] Singh P., Faridi M.S., *Measurement of focal length with phase-shifting Talbot interferometry*, Apllied Optics, Vol. 44, No. 9, 1572-1576 (2005)

Acknowledgements

Firstly, I would like to thank Prof. Dr. R.J. Dwayne Miller from the Max Planck Institute for the Structure and Dynamics of Matter for supervising me as well as Dr. Christian Kränkel from the University of Hamburg for being my second advisor.

Especially I like to thank my group leader Nils-Owe Hansen and my adviser Sebastian Kruber for the great support, helpful ideas and supervising me during the whole project.

Additionally I like to thank Stephanie Uschold and Peter Krötz for supporting advises, inspiring discussions and always nice lunch breaks. Many thanks also to Wesley Robertson, Gourab Chatterjee , Yinfei Lu, Frederik Busse, Cornelius Louwrens Pieterse and Ara Choudhuri for the nice time in the group and helpful advises during the group meetings.
Julian Hirscht, Philipp Pelz and Marcos Atala I give thanks for interesting discussions and advices.

For their technical support I also like to thank Friedjof Tellkamp, Martin Kollewe and Gisbert Mantei and for language refinements I give many thanks to Megan K.T. Nantel. Furthermore, I like to thank all other MPSD members. I had an inspiring time and always good company.

Finally I thank my family and my boyfriend Henning for their unconditional support.

Statement/Erklärung

Hiermit bestätige ich, dass die vorliegende Arbeit von mir selbständig verfasst wurde und ich keine anderen als die angegebenen Hilfsmittel - insbesondere keine im Quellenverzeichnis nicht benannten Internet-Quellen - benutzt habe und die Arbeit von mir vorher nicht einem anderen Prüfungsverfahren eingereicht wurde. Die eingereichte schriftliche Fassung entspricht der auf dem elektronischen Speichermedium. Ich bin damit einverstanden, dass die Masterarbeit veröffentlicht wird.

Ort, Datum	Kristina Strahlendorff